

Tropospheric and Ionospheric Anomalies Induced by Volcanic and Saharan Dust Events as Part of Geosphere Interaction Phenomena

Valerio Tramutoli, Francesco Marchese, Alfredo Falconieri, Carolina Filizzola, Nicola Genzano, Katsumi Hattori, Mariano Lisi, Jann-Yenq y Liu, Dimitar Ouzounov, Michel Parrot, et al.

▶ **To cite this version:**

Valerio Tramutoli, Francesco Marchese, Alfredo Falconieri, Carolina Filizzola, Nicola Genzano, et al.. Tropospheric and Ionospheric Anomalies Induced by Volcanic and Saharan Dust Events as Part of Geosphere Interaction Phenomena. Geosciences, 2019, 9 (4), pp.177. 10.3390/geosciences9040177 . insu-02149766

HAL Id: insu-02149766

https://insu.hal.science/insu-02149766

Submitted on 6 Sep 2019

HAL is a multi-disciplinary open access archive for the deposit and dissemination of scientific research documents, whether they are published or not. The documents may come from teaching and research institutions in France or abroad, or from public or private research centers.

L'archive ouverte pluridisciplinaire **HAL**, est destinée au dépôt et à la diffusion de documents scientifiques de niveau recherche, publiés ou non, émanant des établissements d'enseignement et de recherche français ou étrangers, des laboratoires publics ou privés.

geosciences

MDPI

Article

Tropospheric and Ionospheric Anomalies Induced by Volcanic and Saharan Dust Events as Part of Geosphere Interaction Phenomena

Valerio Tramutoli [1], Francesco Marchese [2,*], Alfredo Falconieri [2], Carolina Filizzola [2], Nicola Genzano [1], Katsumi Hattori [3], Mariano Lisi [1], Jann-Yenq Liu [4,5], Dimitar Ouzounov [6], Michel Parrot [7], Nicola Pergola [2] and Sergey Pulinets [8]

1 School of Engineering, University of Basilicata, 85100 Potenza, Italy; valerio.tramutoli@unibas.it (V.T.); nicogenzano@gmail.com (N.G.); marianoma@blu.it (M.L.)
2 Institute of Methodologies for Environmental Analysis (IMAA), Italian Research Council (CNR), 85050 Tito Scalo (PZ), Italy; alfredo.falconieri@imaa.cnr.it (A.F.); carolina.filizzola@imaa.cnr.it (C.F.); nicola.pergola@imaa.cnr.it (N.P.)
3 Graduate School of Science, Chiba University, Chiba 263-8522, Japan; hattori@earth.s.chiba-u.ac.jp
4 Institute of Space Science, National Central University, Chung-Li 320, Taiwan; tigerjyliu@gmail.com
5 College of Mechanical Engineering and Applied Electronics Technology, Beijing University of Technology, Beijing 100124, China
6 Center of Excellence in Earth Systems Modeling & Observations (CEESMO), Chapman University, Orange, CA 92866, USA; ouzounov@chapman.edu
7 Laboratoire de Physique et Chimie de l'Environnement et de l'Espace, Centre National de la Recherche Scientifique (LPC2E/CNRS), 3A, Avenue de la Recherche Scientifique, 45071 Orléans, France; michel.parrot@cnrs-orleans.fr
8 Space Research Institute, RAS, Space Geophysics, Russian Academy of Sciences, Profsoyuznaya str., 117997 Moscow, Russia; pulse1549@gmail.com
* Correspondence: francesco.marchese@imaa.cnr.it; Tel.: +39-0971427225

Received: 8 February 2019; Accepted: 10 April 2019; Published: 17 April 2019



Abstract: In this work, we assessed the possible relation of ionospheric perturbations observed by Detection of Electro-Magnetic Emissions Transmitted from Earthquake Regions (DEMETER), Global Positioning System total electron content (GPS TEC), National Oceanic and Atmospheric Administration (NOAA)-derived outgoing longwave-Earth radiation (OLR), and atmospheric chemical potential (ACP) measurements, with volcanic and Saharan dust events identified by ground and satellite-based medium infrared/thermal infrared (MIR/TIR) observations. The results indicated that the Mt. Etna (Italy) volcanic activity of 2006 was probably responsible for the ionospheric perturbations revealed by DEMETER on 4 November and 6 December and by GPS TEC observations on 4 November and 12 December. This activity also affected the OLR (on 26 October; 6 and 23 November; and 2, 6, and 14 December) and ACP (on 31 October–1 November) analyses. Similarly, two massive Saharan dust episodes, detected by Robust Satellite Techniques (RST) using Spinning Enhanced Visible and Infrared Imager (SEVIRI) optical data, probably caused the ionospheric anomalies recorded, based on DEMETER and GPS TEC observations, over the Mediterranean basin in May 2008. The study confirmed the perturbing effects of volcanic and dust events on tropospheric and ionospheric parameters. Further, it demonstrated the advantages of using independent satellite observations to investigate atmospheric phenomena, which may not always be well documented. The impact of this increased detection capacity in reducing false positives, in the framework of a short-term seismic hazard forecast based on the study of ionospheric and tropospheric anomalies, is also addressed.

Keywords: lithosphere atmosphere ionosphere coupling; volcanic activity; Saharan dust

1. Introduction

Several literature studies showed that volcanic activity may induce electromagnetic signals (e.g., [1–5]). Among them, a few works were performed using data provided by the Detection of Electro-Magnetic Emissions Transmitted from Earthquake Regions (DEMETER) microsatellite. Zlotnicki et al. [4] investigated the possible occurrence of ionospheric anomalies before volcanic eruptions. The authors analyzed data acquired 30 days before and 15 days after 74 eruptions from 50 volcanoes, recognizing 48 electromagnetic anomalies. In total, they found that ionospheric perturbations, at the satellite altitude, accompanied about 40% of eruptive events. Later on, Zlotnicki et al. [5] extended their analyses with the complete set of DEMETER observations. During the entire mission, 73 volcanoes entered into eruption; for 58 of them, 269 anomalies related to 89 eruptions were detected. Five different types of ionospheric anomalies (density and temperature variations, electrostatic turbulence, and various electromagnetic emissions) were identified. They were similar to those observed above areas of impeding earthquakes. In addition, the study showed the occurrence of volcanic lightning strokes, which were observed by satellite above 12 volcanoes. Rozhnoi et al. [6] reported observations of VLF (Very Low Frequency) waves from a Japanese ground-based transmitter, named JJI, during the January 2011 eruption of Mt. Kirishima (Southern Japan); this volcano was very close to the VLF transmitter. Perturbations of the nighttime subionospheric VLF signal were observed at the time of eruptions (receivers were located in the north of Japan). The authors attributed ionospheric perturbations to the penetration of gravity waves induced by the volcanic activity. Recently, another study investigated physical and chemical climatological anomalies related to volcanic activity, showing their occurrence before some major explosive eruptions [7].

Some studies revealed that aerosols might alter the atmospheric electric field (e.g., [8–10]). Other authors demonstrated the formation of positive anomalies in the ionosphere over Europe, which were correlated with the position of ash clouds from the Eyjafjallajökull (Iceland) volcano [11]. Also, they reported the occurrence of stronger anomalies over Sahara sand storms passing from West Africa through the Atlantic Ocean, proposing the physical mechanism of the formation of ionospheric anomalies, due to modification of troposphere conductivity, within the framework of the global electric circuit (GEC) conception.

In this work, we assessed the impact of Mt. Etna (Sicily, Italy) eruptions and massive Saharan dust outbreaks on the ionosphere. To perform this study, we analyzed a set of heterogeneous observations, spanning from DEMETER data to medium infrared/thermal infrared (MIR/TIR) satellite radiances and Global Positioning System (GPS) measurements. The paper is organized as follows: Section 2 summarizes the main studies of interest for this research; Sections 3 and 4 describe the data and methods used; Section 5 focuses on the achieved results; and Section 6 reports the final remarks of the work.

2. Background

Electrification in dust/sand clouds during storms is a well-known phenomenon in the low terrestrial atmosphere. This phenomenon has been intensively studied because it possibly represents the unique source of electric discharges in the rarefied atmosphere of planets such as Mars [12].

The data showed that dust and sand storms are electrically active. Stow [13] noted that charged particles and aerosols may be separated by gravity within the column of a dust devil. The author observed a field of the order of 20 kV/m above the ground. Charge densities were measured during large dust devils over the Sahara region by Freier [14]; in New Mexico by Crozier [15]; and in the Southwestern United States, as well as in India, by Kamra [16,17]. Wind velocity is a key parameter. Schmidt et al. [18] determined an electric field of 166 kV/m at a 1.7-cm height above a sand dune under the condition of a uniform wind speed of 12 m/s. More recently, Jackson and Farrell [19] measured the horizontal *E*-field in dust devils, finding values up to 120 kV/m (other references can be found in [20]). Zhang et al. [21] performed a wind tunnel experiment simulation for blown sand electrification. They found that, at certain speeds, the maximum average intensity of an electric field at 16 m could

reach 200 kV/m or more. Saunders [22] claimed that inside thunderstorm clouds, the field rarely exceeded 400 kV/m, and that an average value could be of the order of 100 kV/m. Therefore, it is likely that electrostatic discharges could occur at the time of sandstorms.

Concerning volcanic eruptions, these phenomena produce two different types of electromagnetic perturbations in the upper atmosphere. On the one hand, they are sometimes accompanied by lightning strokes, and on the other hand, their effects are similar to explosions (i.e., acoustic-gravity waves are emitted). Volcanic eruptions may perturb the environment up to the ionosphere, owing to the propagation of acoustic-gravity waves (their amplitude increases with the decrease of the density in altitude). Other authors reported some ionospheric variations in the records of HF (High Frequency) Doppler and TEC (Total Electron Content) data, in association with the explosions of Mount Pinatubo on 15 June 1991 [2]. Lightning activities in volcanic plumes have been observed for a long time. There have been, in fact, many reports concerning some spectacular events (e.g., [23–29]), including the April–May 2010 Eyjafjallajökull eruption, which strongly perturbed air traffic (e.g., [30]). Antel et al. [31] showed that the number of whistlers (waves associated to the lightning strokes) observed at Dunedin in New Zealand could be correlated with volcanic activities occurring in the Aleutian Islands, which are the magnetically conjugated region of Dunedin. However, lightning activity is not always observed during volcanic eruptions, and some studies have been undertaken to understand this phenomenon. James et al. [32] performed some experiments to simulate the electrification mechanism of ash. They showed that the dominant charging process occurs during the fracture of silicate particles (see also [33]). Mather and Harrison [34] suggested that the ash fragmentation mechanism is a key parameter. During the aforementioned Eyjafjallajökull eruption, some authors noticed a change in the lightning activity [35]. They attributed this effect to a temperature change at the top of the plume. McNutt and Williams [36] intensively studied the occurrence of lightning activity as a function of many parameters (e.g., Volcanic Explosivity Index—VEI, ash plume height, magma composition, latitude of volcanoes, and season during many different eruptions), emphasizing the important role of water vapor. Finally, another work demonstrated the impact of dust aerosols on the ionosphere because of an electromagnetic coupling mechanism based on a drop of column electric conductivity [11].

3. Data

3.1. DEMETER

DEMETER was a low-altitude satellite (710 km) launched in June 2004 into a polar and circular orbit. The altitude of the satellite was decreased to 660 km in December 2005. The scientific mission of DEMETER ended in December 2010. The orbit of DEMETER was nearly sun-synchronous and the up-going half-orbits corresponded to nighttime (10:30 p.m. LT), whereas the down-going half-orbits corresponded to daytime (10:30 a.m. LT). The main scientific objectives of DEMETER were to study the disturbances of the ionosphere due to seismo-electromagnetic effects and anthropogenic activities (power line harmonic radiation, VLF transmitters, and HF broadcasting stations). For this purpose, DEMETER measured the electromagnetic waves and plasma parameters all around the globe, except in the auroral zones. Regarding the wave experiment, the VLF range for the electric field was from DC up to 20 kHz. There were two scientific modes: a survey mode where spectra of one electric component were onboard computed up to 20 kHz (time resolution of 2 s and frequency resolution of 20 Hz), and a burst mode where, in addition to the onboard computed spectra, waveforms of the same electric field component were recorded up to 20 kHz. Details of the electric field experiment can be found in [37]. The electron density was measured by the experiment ISL (Instrument Sonde de Langmuir; [38]), whereas the ion density was given by the experiment IAP (Instrument d'Analyse du Plasma; [39]).

3.2. AVHRR and SEVIRI

The Advanced Very High Resolution Radiometer (AVHRR), flying aboard the National Oceanic and Atmospheric Administration (NOAA) and Meteorological Operational Satellite (METOP) polar satellites, was designed mainly for meteorological studies.

This instrument, which offers a good trade-off between temporal (up to 6 h) and spatial (1.1 km at nadir view) resolution, provides data in five spectral channels ranging from visible (VIS) to thermal infrared (TIR). Channel 3 (3.55–3.93 μm), which is centered in the medium infrared region (MIR), has been largely used to identify volcanic thermal anomalies, such as lava flows and fumarolic emissions (e.g., [40–44]). Channel 4 (10.3–11.3 μm), which is located in the TIR region, has been used in combination with channel 5 (11.5–12.5 μm) to detect ash/dust clouds by exploiting the reverse absorption effects of silicate particles at 11- and 12-μm wavelengths in comparison with water/ice droplets [45,46].

Spinning Enhanced Visible and Infrared Imager (SEVIRI), aboard Meteosat Second Generation (MSG) satellites, operates in 12 spectral channels, providing data with a temporal sampling of 15 min. Despite the coarse spatial resolution (~3 km at the nadir), this sensor represents, thanks to its geostationary attitude, an important instrument for studying, monitoring, and characterizing both volcanic phenomena (e.g., [47–49]) and Saharan dust events (e.g., [50–52]).

In this work, we present the results achieved from analyzing a set of satellite-based products generated using the robust satellite technique (RST) multitemporal approach [53,54]. In addition, we investigated the AVHRR observations of Outgoing Longwave-Earth radiation (OLR) associated with the Mt. Etna eruptive activity of September–December 2006, available from the NOAA Climate Prediction Center.

3.3. GPS TEC

The GPS consists of 24 satellites, evenly distributed in six orbital planes around the globe, at an altitude of about 20,200 km. The ionosphere is a dispersive medium for GPS signals ($f1$ = 1575.42 MHz and $f2$ = 1227.60 MHz) in the microwave band. Therefore, signals traveling through this medium are affected proportionally to the inverse of the square of their frequencies. This effect can reveal information about the parameters of the ionosphere in terms of the TEC of a slant path, which is the integral of the electron density between a ground-based receiver and an associated GPS satellite. From the broadcast ephemeris (e.g., satellite time, elevation, and location) and a given ionospheric (shell) height at about 350 km altitude [55], the slant TEC along the ray path can be converted, usually using a simple cosine function of the satellite zenith into the vertical TEC (VTEC, for simplicity hereafter, TEC) at its associated longitude and latitude [56,57]. Since each receiver could simultaneously trace up to 10 or more GPS satellites, a regional image over the local network area can be constructed by about 10 times the receiving points every 30 s.

4. Methods

4.1. DEMETER Methodology

Global maps of the ionospheric density observed by DEMETER were obtained to study this parameter as a function of locations, seasons, local time, and magnetic activity. They showed that, in the case of low magnetic activity ($K_p < 3$) the ionospheric density has large-scale variations. Then, a simple comparison between the amplitude of a localized perturbation and a background-averaged value obtained in similar conditions was used to reveal an anomalous variation. An extended description of the methodology used to identify ionospheric anomalies in DEMETER records can be found in some previous literature works [58–60].

4.2. RST Approach

The RST approach was developed to study and monitor several natural/environmental hazards, such as earthquakes, floods, oil spills, forest fires, and volcanic activity (e.g., [61–67]).

In more detail, RST considers every anomaly in the space-time domain as a deviation from a normal state that may be determined by processing multiannual time series of homogeneous (i.e., same calendar month and overpass time) cloud-free satellite records [54]. The Absolutely Local Index of Change of Environment (ALICE) index was used to identify anomalous variations of the signal related to possible perturbing events:

$$\otimes_V (x, y, t) = \frac{V(x, y, t) - \mu_V(x, y)}{\sigma(x, y)} \quad (1)$$

where $V(x, y, t)$ is the satellite signal measured at time t in a specific spectral band or band combination at the same location (x, y), and $\mu_V(x, y)$ and $\sigma_V(x, y)$ stand for the temporal mean and standard deviation of $\mathrm{V}(x, y, t)$.

The $\mathrm{RST_{VOLC}}$ and $\mathrm{RST_{ASH}}$ algorithms are two RST configurations specifically developed for volcanological applications. $\mathrm{RST_{VOLC}}$ jointly uses the $\otimes_{MIR}(x, y, t)$ and $\otimes_{MIR-TIR}(x, y, t)$ indices to detect volcanic hot spots [42]. The first one analyzes the MIR signal (i.e., $\mathrm{V}(x, y, t) = BT_{MIR}(x, y, t)$), the second one the difference of MIR and TIR (around 11 µm) brightness temperatures (i.e., $\mathrm{V}(x, y, t) = BT_{MIR}(x, y, t) - BT_{TIR}(x, y, t)$).

$\mathrm{RST_{ASH}}$ combines the $\otimes_{TIR}(x, y, t)$ and $\otimes_{MIR-TIR}(x, y, t)$ indices to identify volcanic ash clouds [68]. The $\otimes_{\Delta TIR}(x, y, t)$ index, which analyzes the difference of brightness temperatures measured in the TIR band at around 11- and 12-µm wavelengths ($\mathrm{V}(x, y, t) = BT_{11}(x, y, t) - BT_{12}(x, y, t)$), is also sensitive to airborne dust [52]. Hence, it can be used for investigating Saharan dust outbreaks even in combination with other RST indices, as performed in [68].

4.3. Analysis of OLR Anomalies

One of the main parameters used to characterize the Earth's radiation environment is the OLR. The latter has been associated with the top of the atmosphere (TOA), integrating the longwave radiation (LWR) emissions between 10 and 13 microns from the ground, lower atmosphere, and clouds. Hence, it has primarily been used to study Earth's radiative budget and climate. An increase in radiation and a transient change in OLR was proposed to be related to thermodynamic processes in the atmosphere over major geohazard regions [69–71]), and the anomalous trend was measured as an OLR anomaly. The latter was defined similarly to the anomalous thermal field definition proposed by Tramutoli et al. [72,73] and represents the different amplitude for a specific spatial location and predefined times:

$$OLR\ anomaly\ (x, y, t) = \frac{S(x, y, t) - \overline{S}(x, y, t)}{\tau(x, y, t)} \quad (2)$$

$$\overline{\mathrm{S}}(x, y, t) = \frac{1}{\mathrm{N}} \sum_{\mathrm{i}=1}^{\mathrm{N}} S(x_i, y_i, t_i) \quad (3)$$

$$\tau(x, y, z) = \sqrt{\frac{\sum \left(S(x, y, t) - \overline{S}(x, y, t)\right)^2}{\mathrm{N}}} \quad (4)$$

where $S(x, y, t)$ is the current OLR value; $\overline{S}(x, y, t)$ is the computed mean of the background field, defined as the daily mean value of OLR $S\left(x_i, y_i, t_j\right)$ over an area of longitude x and latitude y in the *t-th* day of M years; and $\tau(x, y, z)$ is the standard deviation over the same location (x, y) and local time (t) as the OLR value.

The first result in connecting the LWR variations in relation to volcanic activity was obtained for the Mt. Kirishima (Japan) eruption of 26–30 January 2011 [6,71]. An abnormal increase in the thermal

radiation was detected around 22 December 2010 (i.e., about one month before the aforementioned eruption), and the maximum was observed from 22 to 30 January 2011, which coincided with the peak of volcanic activity.

4.4. Analysis of GPS TEC Anomalies

Usually, for the full constellation, a ground-based receiver can simultaneously record signals from more than 10 GPS satellites [56]. Therefore, for a network of n ground-based GPS receivers, an image over the network area with about 10n TEC points can be constructed every 30 s. Similarly, based on measurements of worldwide limited hundreds of ground-based receivers of the International GNSS Service (IGS), the global ionosphere map (GIM) of the TEC has been daily and routinely published by the Center for Orbit Determination in Europe (CODE), European Space Operations Centre (ESOC), University of Warmia and Mazury (UWM), NASA's Jet Propulsion Laboratory (JPL), and Technical University of Catalonia (UPC) (ftp://cddis.gsfc.nasa.gov/gps/products/ionex/) to estimate ionospheric effects on radio propagation geodesy applications since 1998 [74]. Currently, the GIM is routinely published in a 1- or 2-h time interval with 1–2 days delay. The spatial resolutions of the GIM on the ±87.5°N latitude and ±180°E longitude are 2.5° and 5°, respectively. Thus, a local network of ground-based receivers is useful to monitor the fine structure of the TEC over the network area (a small region, such as that affected by a volcanic eruption), while the GIM is suitable to observe the relatively large structure of the TEC (a larger area, such as that affected by a dust event). Specific methodologies were developed to detect anomalies of GPS TEC signals. They were applied here to help in interpreting DEMETER observations.

4.5. Atmospheric Chemical Potential (ACP) Correction Approach

A physical model of thermal anomalies registered before earthquakes and around the time of volcano eruptions would explain that, due to air ionization by radon emanating from the active faults, the newly formed ions become the centers of water vapor nucleation and formation of the large ion clusters [75]. The bond energy of water molecules with ions is larger than that in pure water drops, where it is equal to the latent heat energy per one molecule U = 0.422 eV, which is equal to the water molecule chemical potential. The higher the ion production rate and concentration of ions, the higher the bond energy of water molecules with ions (i.e., the chemical potential). The process of evaporation/condensation, which is the phase transition of the first order, always takes place during the chemical potential equality. However, newly formed ions created by ionization have a different chemical potential, which is what we took into account. In the one-component approximation, we introduced the correction to the chemical potential ΔU, which takes into account this circumstance. In this case, the real chemical potential can be expressed as

$$U(t) = U_0 + \Delta U cos2t \tag{5}$$

where U_0 is the chemical potential for pure water, and $U(t)$ is the chemical potential where ionization and hydration are taken into account. By $cos2t$, we take into account the daily changes of the solar radiation. The changes of the chemical potential under action of ionization will affect the relative humidity H, which can be estimated using the parameter ΔU:

$$H(t) = \frac{\exp\left(\frac{-U(t)}{kT}\right)}{\exp\left(\frac{-U_0}{kT}\right)} = \exp\left(\frac{U_0 - U(t)}{kT}\right) = \exp\left(-\frac{0.032\ \Delta U cos^2 t}{(kT)^2}\right) \tag{6}$$

where k is the Boltzmann constant, and T is the air temperature. The changes of the chemical potential can be then derived from the formula above by using the satellite microwave sounders data on vertical profiles of the air temperature and relative humidity.

5. Analyzed Events

5.1. Mt. Etna Activity of November–December 2006

Mt. Etna is the largest and most active volcano on land areas in Europe. Strombolian activity, lava fountains, and emission of lava flows frequently occur at the summit craters (e.g., [76,77]). Flank eruptions, which are often associated with weak explosive activity (e.g., [78]), are generally less frequent. Nonetheless, they pose a serious threat to inhabited areas [79], since they are capable of emitting lava bodies extending for several kilometers in length (e.g., [80]). In recent years, some intense eruptive events occurred at Mt. Etna; they were widely investigated from space by means of the RST technique (e.g., [41,44]). Among them, eruptions of November–December 2006 were preceded by a significant lava effusion of short-time duration, occurring during 14–24 July 2006 [81], and by a number of paroxysms which took place from the Southeast Crater (SEC) [82]. In particular, during 22 September–4 November 2006, lava flows were emitted by multiple vents located along fractures on the SEC [83], while from 8 November to 14 December, several Strombolian explosions and ash emissions were recorded [84]. On 6 December 2006, an ash plume was emitted reaching, in the early morning of the same day, an altitude of 3.6–4.6 km above sea level (a.s.l.) [85].

5.2. Saharan Dust Events of May 2008

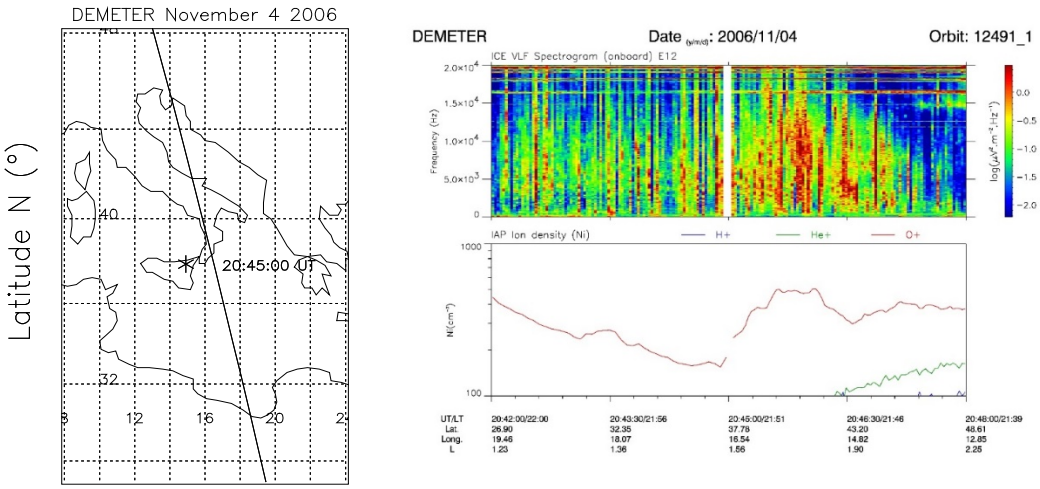
During 18–23 May 2008, a long-lasting dust phenomenon coming from Algeria and Tunisia (North Africa) affected both the Mediterranean basin and Europe. Specifically, on 18 May, airborne dust dispersed over Italy and Central Europe. Dust coverage then affected Eastern Europe, extending up to an altitude of 3–5 km a.s.l. over Greece on 20 May. In the following days, the dust concentration gradually decreased [86]. However, at the end of same month (i.e., during 26–31 May), another intense dust episode, affecting once again Europe and part of the Mediterranean region, occurred (e.g., [87–89]). We investigated the impact of the abovementioned Saharan dust events, as well as of Mt. Etna eruptions described in the previous paragraph, on the ionosphere. Results of these analyses are shown and discussed in the next section.

6. Results

6.1. Ionospheric Perturbations of November–December 2006

Figure 1 shows the DEMETER data of 4 November 2006 recorded along the satellite orbit track intersecting part of Italy, the Mediterranean Sea, and North Africa (see Figure 1a). Specifically, Figure 1b displays an electric field spectrogram up to 20 kHz (see top panel) showing the increase of the whistler intensities (each vertical line corresponds to a lightning stroke and is called a whistler) over the Mediterranean Sea. In the spectrogram, the horizontal lines above 15 kHz were due to the VLF ground-based transmitters.

The increase of whistler intensities recorded by DEMETER revealed an important increase of the ion density at the Mt. Etna latitude, as shown in the bottom panel of Figure 1b. Figure 2 displays the AVHRR imagery of November 4 2006 at 20:44 UT, which was close in time to the aforementioned DEMETER observation, magnified over the target area. The figure shows that some image pixels, i.e., those located over Mt. Etna area (see pixels in bright tones), were significantly more radiant than the neighbor ones in the MIR band. RST_{VOLC} considered most of those pixels as anomalous (see the red ones on hot spot map shown in the figure inset), revealing the occurrence of an intense thermal volcanic activity at the time of DEMETER observation. Figure 3 displays the RST_{ASH} map from same AVHRR data, showing that weak ash emission also possibly occurred on that day (see pixels depicted in red within the yellow square indicating Mt. Etna area). It is worth noting that RST_{ASH} flagged some ash pixels also SE of Sicily (Southern Italy). Since those pixels were sparsely distributed, we can hypothesize that a thin dust layer also affected the scene.



(**a**) (**b**)

Figure 1. (**a**) Orbit track of Detection of Electro-Magnetic Emissions Transmitted from Earthquake Regions (DEMETER) on 4 November 2006 with indication of time of the pass at the Mount Etna latitude. (**b**) On the top, electric VLF (Very Low Frequency) spectrogram from 0 up to 20 kHz, with its intensity color coded according to the scale on the right, referring to DEMETER data recorded between 8:42:00 and 8:48:00 p.m. UT; on the bottom, variation of the O+ ion density (the densities of the other ions are much lower) with the parameters displayed below representing the time in UT and LT, the geographic latitude and longitude, and the McIlwain parameter L.

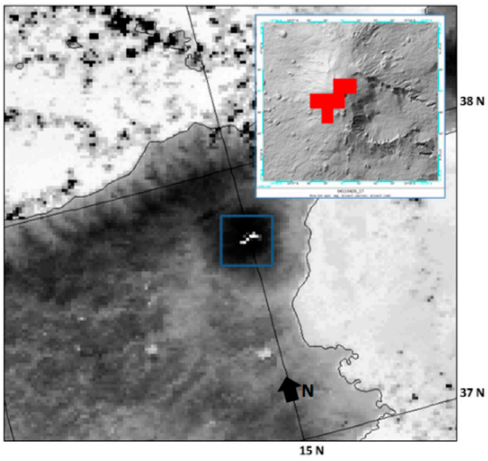


Figure 2. Advanced Very High Resolution Radiometer (AVHRR) channel 3 (medium infrared (MIR)) image of 4 November 2006 at 8:44 p.m. UT in Lambert Azimuthal Equal Area (LAEA) projection, with indication of Mt. Etna area (see blue square). The right top panel of the figure displays the hot spot map reporting anomalous pixels (in red) detected by RST_{VOLC} (with $\otimes_{MIR}(x,y,t) > 3$ *AND* $\otimes_{MIR\text{-}TIR}(x,y,t) > 3$).

Figure 4 displays the DEMETER data of 6 December 2006. In particular, the top panel represents the spectrogram of an electric component up to 20 kHz, whereas the bottom panel shows the variation of the density of the ion O+ density along the satellite orbit. Looking at the figure, one can see some lightning activities (i.e., vertical lines in the spectrogram), but above all, an increase of the ion density when the satellite was at the latitude of the Mt. Etna area (i.e., at around 8:45 p.m. UT). Figure 5 shows the RST_{ASH} product of 6 December at 12:37 p.m. UT revealing the presence of an ash plume, which was partially identified by satellite because of low ash concentration (e.g., [90]), dispersing from Mt. Etna area towards Mediterranean Sea. The plume ideally crossed the DEMETER ground track (see the blue line in Figure 5) some hours before the observation of ionospheric disturbances at 8:45 p.m. UT,

shown in Figure 4. It is worth mentioning that the volcanic activity was still in progress at the time of DEMETER observation, as indicated by the RST_{VOLC} map of 8:02 p.m. UTC, which is not shown here.

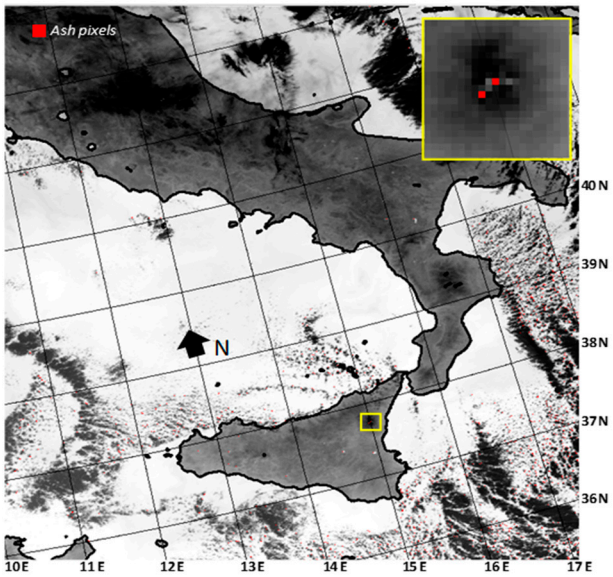


Figure 3. AVHRR channel 4 (thermal infrared (TIR)) image of 4 November 2006 at 8:44 p.m. UT in LAEA projection; ash pixels detected by RST_{ASH} (with $\otimes_{\Delta TIR}(x,y,t) < -2$ *AND* $\otimes_{MIR\text{-}TIR}(x,y,t) > 1$) are depicted in red and magnified at the top right-side of the figure (see yellow square).

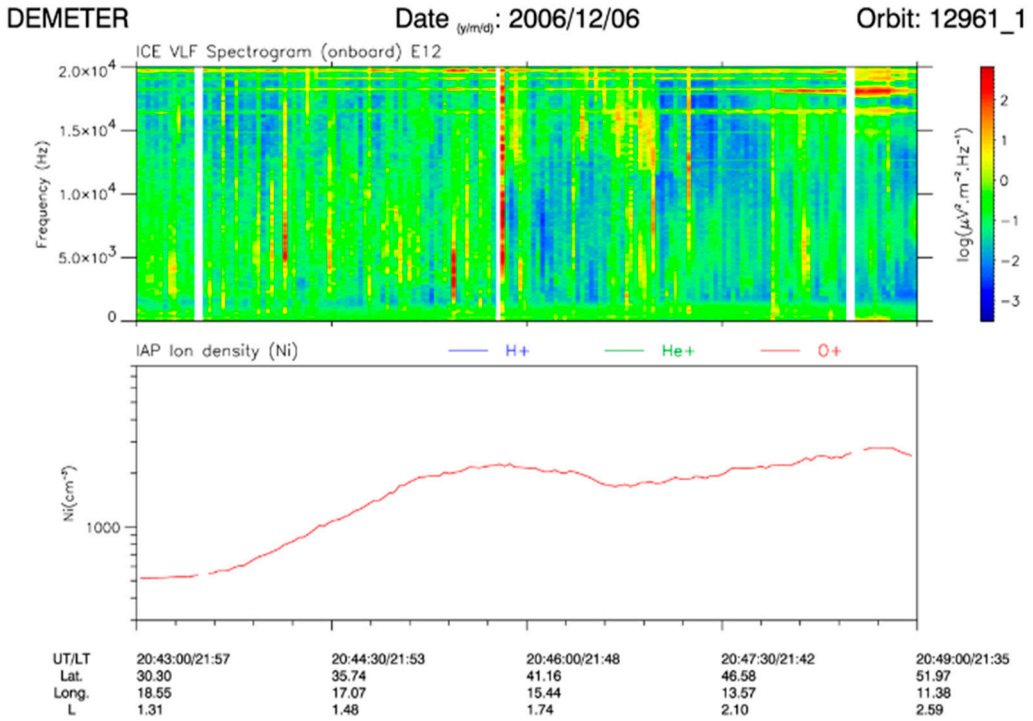


Figure 4. DEMETER data recorded on 6 December 2006 between 8:43:00 and 8:49:00 p.m. UT. On the top, electric VLF spectrogram from 0 up to 20 kHz with its intensity color coded according to the scale; on the bottom, variation of the ion O+ density (the densities of the other ions are much lower), with the parameters displayed below having the same meaning as Figure 1.

The analyses performed above indicated that Mt. Etna eruptive activity possibly perturbed the ionosphere. As a further evidence of this hypothesis, Figure 6a displays the continuous monitoring of

OLR over the monitored volcanic area, obtained from the analysis of NOAA-15 AVHRR nighttime data (with 1 × 1-degree resolution) during the period of 1 September–31 December 2006.

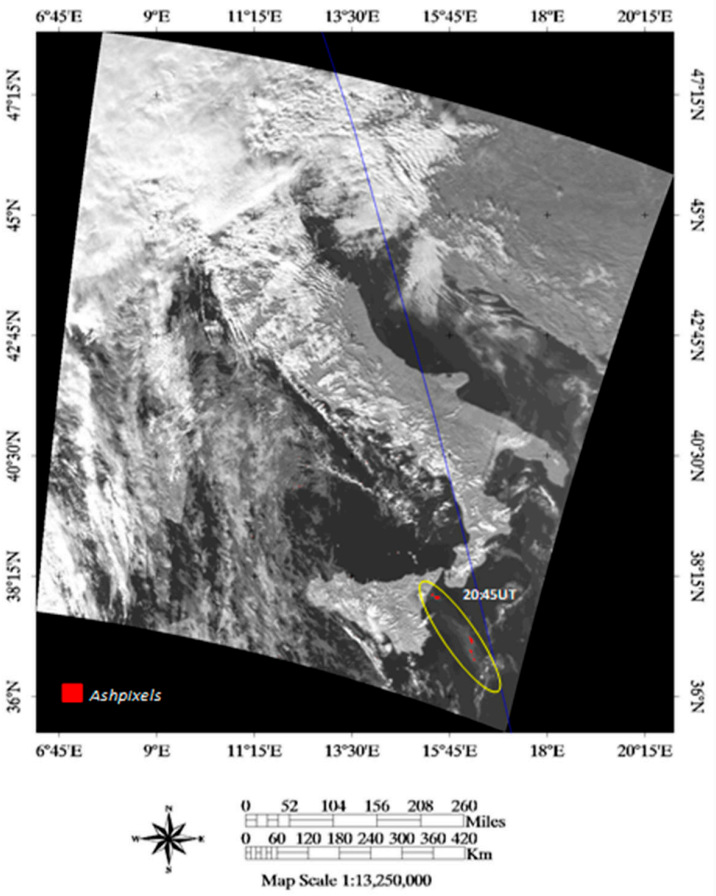


Figure 5. RST_{ASH} product generated from AVHRR data of 6 December 2006 at 12:37 p.m. UT. Ash pixels are depicted in red (the visible channel shown in background was used in detection phase for better filtering clouds; e.g., [91]). The blue line is the DEMETER orbit ground track.

The plot shows the thermal enhancement time (red columns) at TOA (at 8:00 p.m. LT) during the Mt. Etna eruptions (grey boxes). Mean daily nighttime values (black curve) show the climatological trend (decrease) for the winter season. Distinctive anomalies were observed on 26 October; 6 and 23 November; and 2, 6, and 14 December. For comparison, the same calculations for one year later (September–December 2007) of OLR daily nighttime values (yellow columns) were included. No significant anomalies were observed for 2007, except for the single large anomaly recorded in September 2007, which was probably associated with the significant eruption registered for the same period. For the rest of the period in 2007, sporadic and less intense eruptive activity occurred; therefore, no significant thermal anomaly at TOA was registered.

As an additional parameter for this analysis, we computed the correction into the ACP. This parameter shows the ionization rate change in the lower atmosphere [75].

The 2006 ACP for the same period (pinks line) followed the OLR trend and in values were smaller than 2007, the period with no eruptions (cyan). Thus, the heat released from the volcano vents associated with eruption activities, showing synchronization with thermal anomaly occurrences, altered the ACP in 2006. Additionally, Figure 6b,c show the 2D maps of the anomaly intensities represented by the OLR *E*-index. Only positive values are shown, revealing that more intense OLR anomalies were located over the Mt. Etna area. Finally, the OLR thermal anomaly generation initiated a chain of other effects in atmosphere, reaching the altitudes of the upper atmosphere and ionosphere. The temporal evolution of the chemical potential shown in Figure 7a for the period 10 October–30

December 2006 revealed the maximum value four days before the eruption onset marked by the red arrow. Those measurements were taken exactly at the Mt. Etna location. In addition, Figure 7b displays the 2D distributions of ACP over Southern Italy for the period 30 October–1 November, when the mean peak in the time series of ΔU was recorded. On 30 October at 6:00 p.m. UT, a yellow spot affected the monitored volcano. On 31 October at 12:00 a.m. UT, it extended in longitude over almost all of Sicily. The same day at 6:00 a.m. UT, the signal intensity increased; at 12:00 p.m. UT, we observed the signal only over the volcanic area, but at the same time, ΔU increased over Southern Italy. Then, on the next two intervals, the signal expanded again to disappear at 12:00 p.m. UT on 1 November.

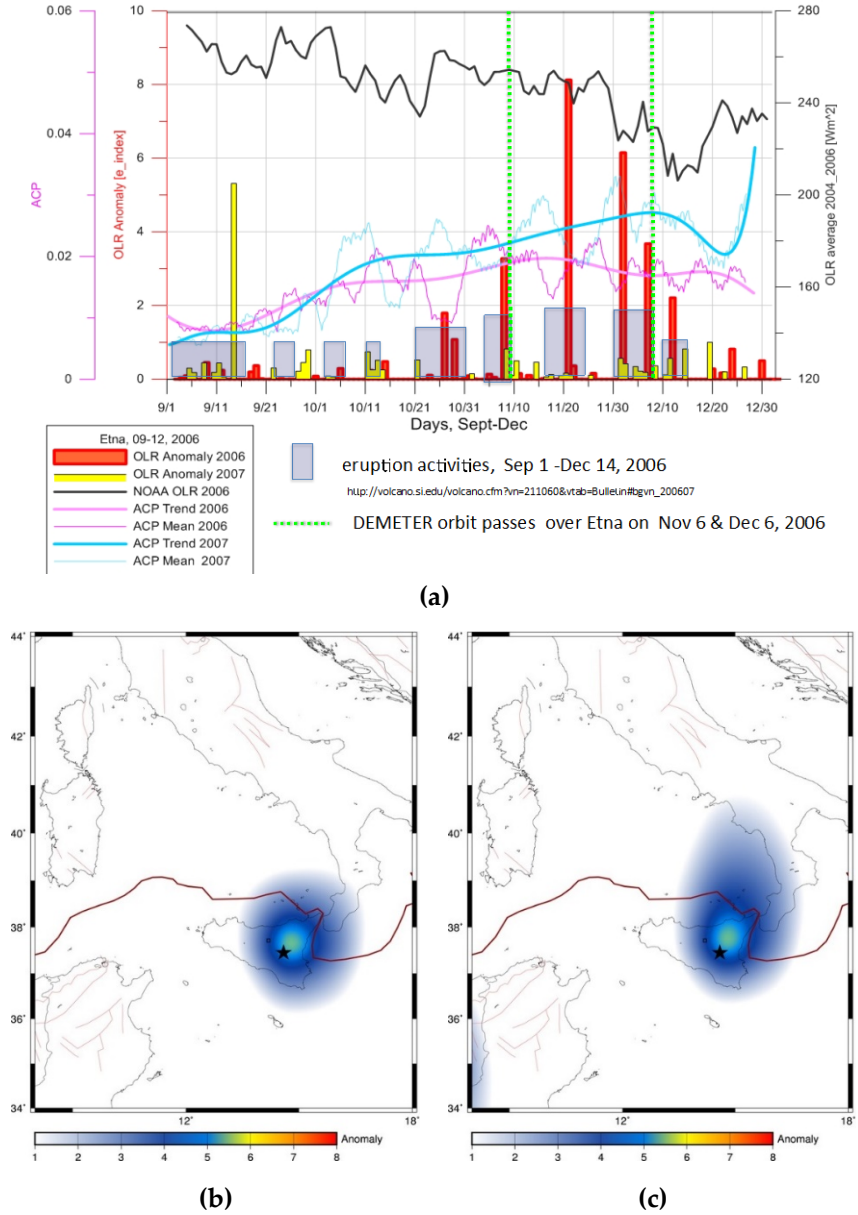


Figure 6. (**a**) Daily nighttime National Oceanic and Atmospheric Administration (NOAA)-AVHRR outgoing longwave-Earth radiation (OLR) anomalous values over Mt. Etna area during September–December 2006, with OLR average values for 2006 (black), OLR anomalies for 2006 (red column), OLR anomalies for 2007 (yellow columns), atmospheric chemical potential (ACP) for 2006 (pink), ACP for 2007 (cyan), Etna 2006 eruptions (grey boxes), and DEMETER orbits (dash green). (**b**) Daily maps for 6 November 2006 representing the OLR anomalies' spatial extent over Etna regions (with black star—Etna volcano, red solid lines—plate boundaries, brown lines—fault systems). (**c**) Daily maps for 6 December 2006 (see previous point).

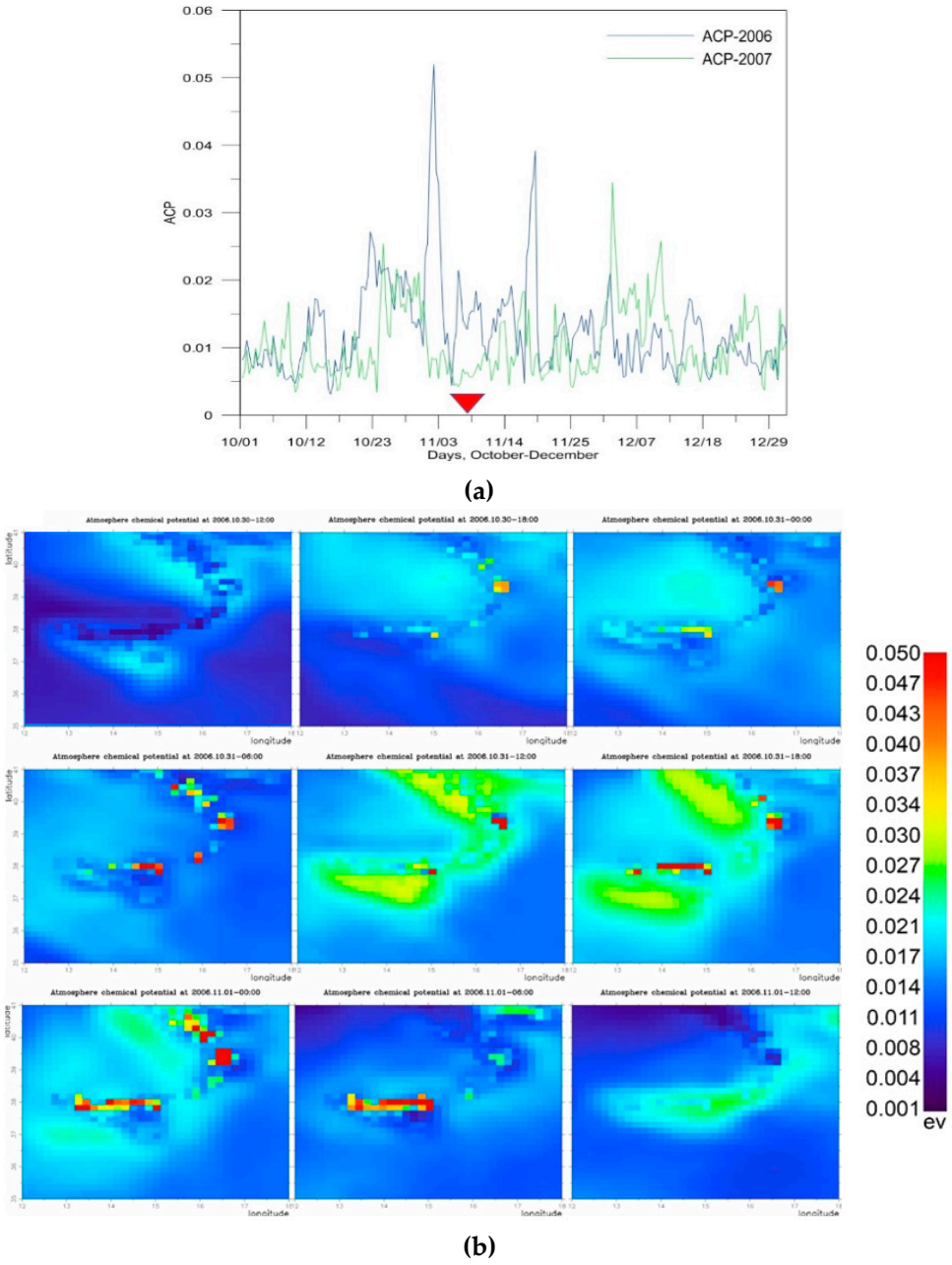
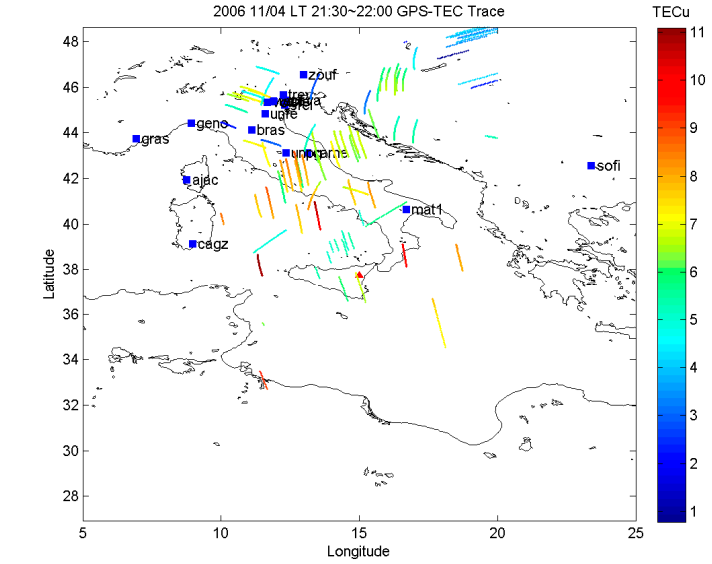


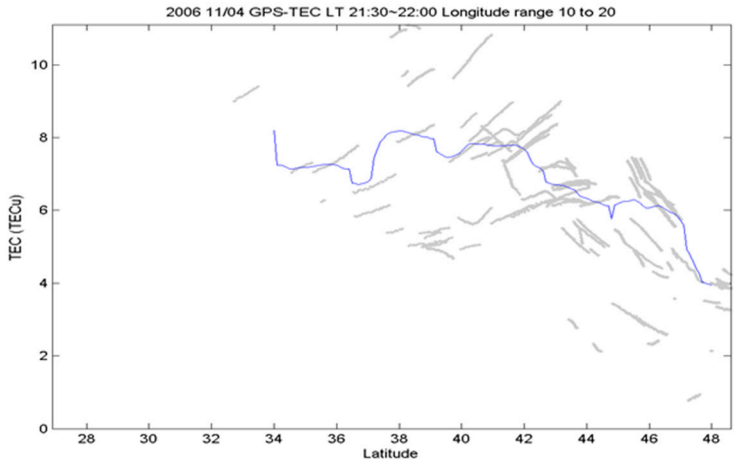
Figure 7. (**a**) Temporal dynamics of the chemical potential correction ΔU over the Etna volcano (37.755N, 14.995E) for the period 10 October–30 December 2006; red arrow indicates the 4 November 2006 eruption; (**b**) 2D distributions of the chemical potential correction for the period 30 October–01 November 2006.

For cross-comparison with the ion density increase observed by DEMETER at the latitude of Mt. Etna, a local network of 17 ground-based GPS receivers in the volcano region was used to derive the ionospheric TEC during 9:30–10:00 p.m. LT on 4 November 2006 (see Figure 8a).

Figure 8b shows that the TEC prominently increased between 37° and 42° N, in good agreement with the ion density increase probed by DEMETER. Similarly, the ion density recorded along the DEMETER satellite orbit over Mt. Etna area prominently increased on 6 December 2006 at around 8:45 p.m. UT, in concomitance with the increase of the ground-based TEC derived by the local GPS receiver network (Figure 9a) at the volcano longitude (see Figure 9b). Thus, DEMETER ion observations and ground-based GPS TEC simultaneously increased over the Mt. Etna area during the nighttime period on both eruption days.



(a)



(b)

Figure 8. (**a**) Locations of 17 ground-based Global Positioning System (GPS) receivers (SOPAC, http://sopac.ucsd.edu/) and their GPS total electron content (TEC) ground traces during 9:30–10:00 p.m. on 4 November 2006. Blue squares and color curves in the top panel stand for the ground-based GPS receivers and the TEC at its associated ionospheric point, respectively. (**b**) GPS TEC variations along the volcano longitude during 9:30-10:00 p.m. LT on 4 November 2006. Grey and blue curves in the bottom panel denote the GPS TEC in the network and their median within 10–20 longitude (with a 0.1-deg latitudinal grid), respectively.

6.2. Ionospheric Perturbations of May 2008

During May 2008, DEMETER recorded a significant number of ionospheric anomalies over the Mediterranean basin. Figure 10 shows an example of DEMETER records for 19 May 2008, displaying a spectrogram of one electric field component up to 20 kHz and the variation of the electron density along the orbit track, in red, intersecting the region extending from Central Europe to Libya between 8:08:30 and 8:10:45 p.m. UT (Figure 11a). Ionospheric disturbances were recorded by DEMETER in concomitance with some eruptive activities that were in progress at the Mt. Etna and Stromboli volcanoes (Aeolian Islands; Italy) [92–94]. However, RST_{ASH} products from AVHRR observations as well as a visual inspection of satellite imagery did not reveal any significant presence of airborne ash. Hence, ionospheric anomalies were not ascribable to volcanic phenomena even because of the

large spatial distance of the DEMETER orbit track from eruptive centers. On the other hand, two intense Saharan dust events affected Europe and the Mediterranean basin in May 2008 (see Section 5.2), prompting us to assess their possible impact on the ionosphere.

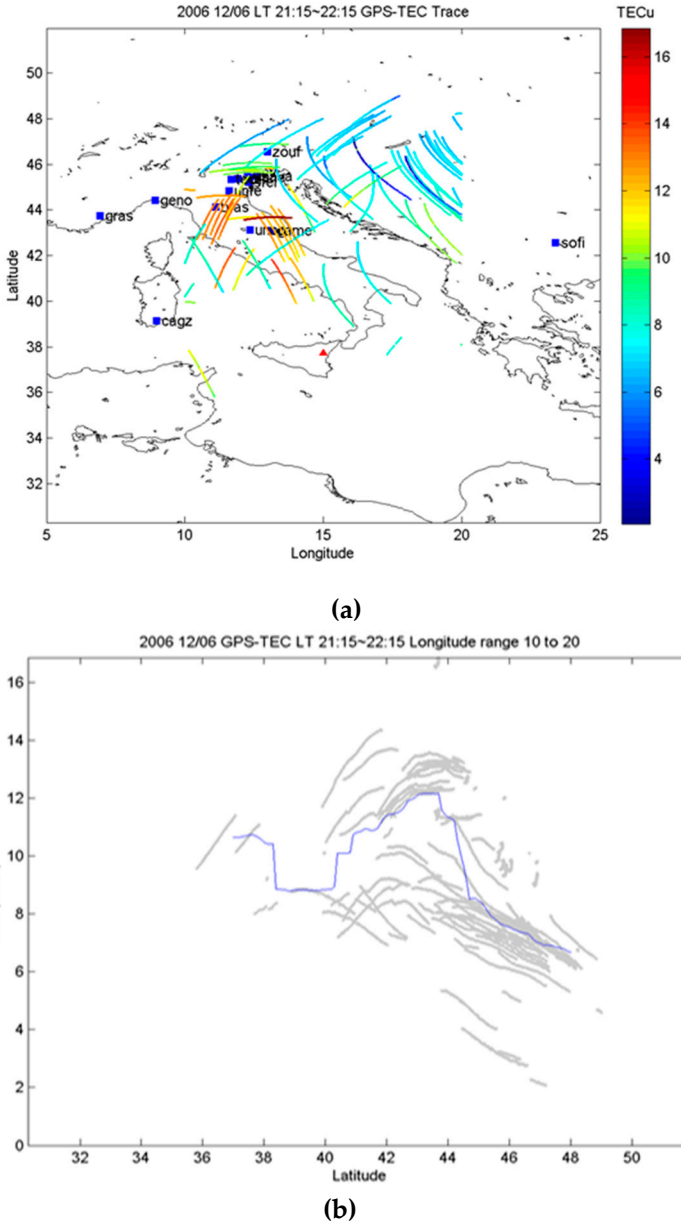


Figure 9. (**a**) Locations of 15 ground-based GPS receivers and their GPS TEC ground traces during 9:30–10:00 p.m. LT on 6 December 2006; (**b**) GPS TEC variations along the volcano longitude during 9:30–10:00 p.m. on 6 December 2006.

Figure 11 displays the horizontal (i.e., 2D) distribution of airborne dust (in different shades of brown) over Europe and part of the Mediterranean basin retrieved from nighttime SEVIRI data of 19 and 20 May 2008 using the RST method. In detail, Figure 11a shows the RST map of 19 May at 8:00 p.m. UT, revealing the presence of dust coverage affecting part of the Mediterranean Sea and Eastern Europe.

The dust plume, which was presumably spatially more extended than that indicated by Figure 11a, due meteorological clouds masking the underlying dust layer (see black/dark grey pixels on the TIR channel displayed in background), affected part of the Mediterranean Sea and Greece. Figure 11b,

referring to the map of 20 May at 12:00 a.m. UT, showed that some hours after previous satellite observation, the dust phenomenon still affected the aforementioned areas. To assess the identification of airborne dust in Figure 11, we analyzed the total attenuated backscatter profile at 532 nm, acquired on 20 May between 12:29 and 12:43 a.m. UT along the orbit track of Cloud-Aerosol Lidar and Infrared Pathfinder Satellite Observation (CALIPSO). The latter uses an active lidar instrument and passive infrared/visible imagers to probe the vertical structure and properties of thin clouds and aerosols over the globe [95].

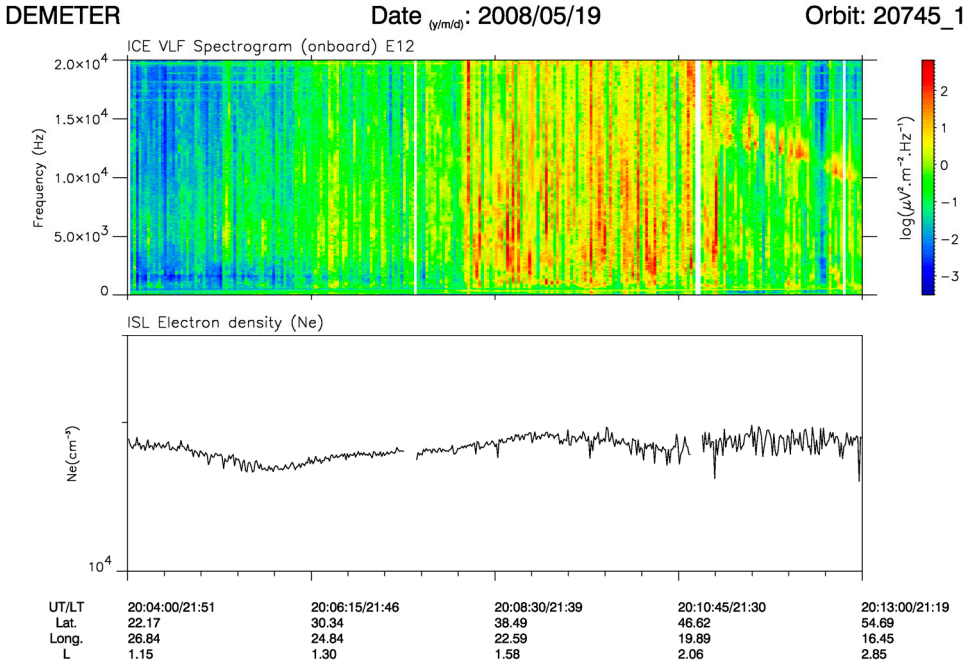


Figure 10. DEMETER data recorded on 19 May 2008 between 8:04:00 and 8:13:00 p.m. UT. On the top, electric VLF spectrogram from 0 up to 20 kHz with its intensity color coded according to the scale on the right; on the bottom, variation of the electron density.

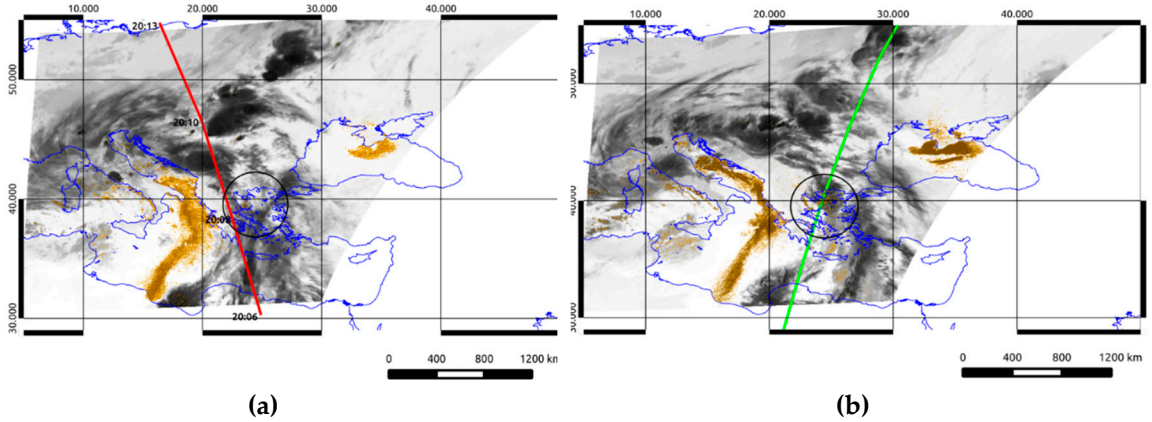
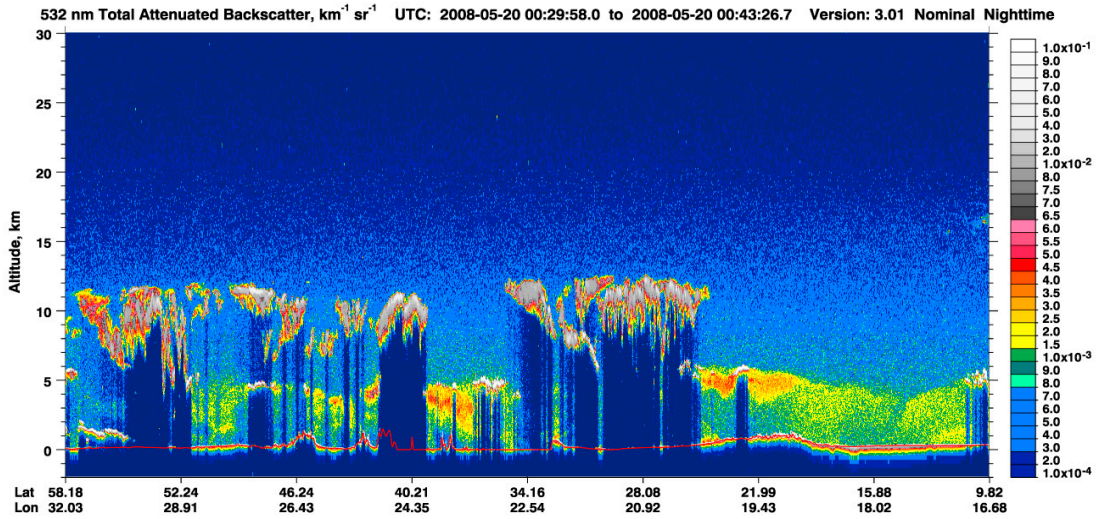


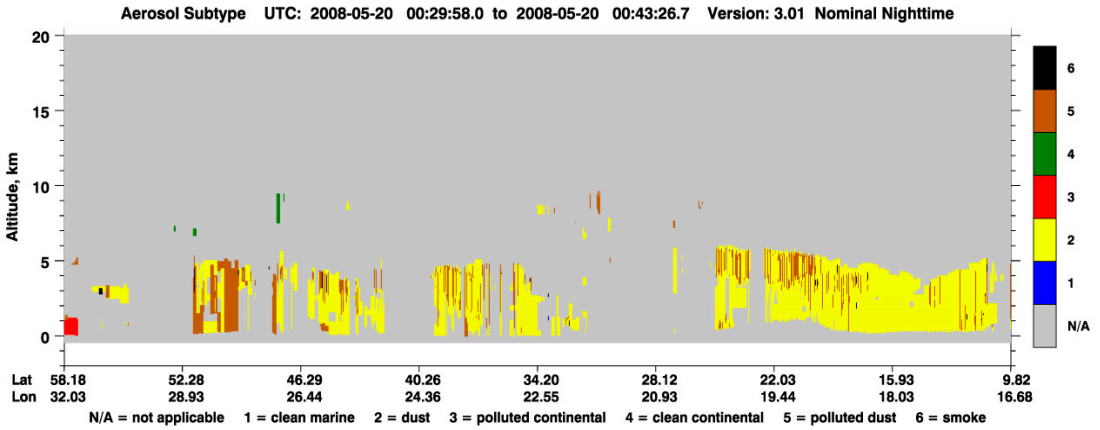
Figure 11. Robust satellite technique (RST) dust maps; pixels in different shades of brown indicate regions less (i.e., $\otimes_{\Delta TIR}(x,y,t) < -2$; light brown) and more affected by dust (i.e., $\otimes_{\Delta TIR}(x,y,t) < -3$; medium brown). (**a**) 19 May 2008 at 8:00 p.m. UT; (**b**) 20 May 2008 at 12:00 a.m. UT. Red (top panel) and green (bottom panel) lines on top and bottom panels are the ground track of DEMETER and Cloud-Aerosol Lidar and Infrared Pathfinder Satellite Observation (CALIPSO) orbits, respectively. The SEVIRI TIR channel, at 11-μm wavelength, is displayed in the background.

Figure 12 displays the Cloud-Aerosol Lidar with Orthogonal Polarization Lidar (CALIOP) lidar profile, showing the presence of an aerosol layer over the region marked by the black ellipse (see top

panel), where RST flagged a number of dusty pixels. The aerosol subtype profile reported in the bottom panel (see Figure 12b) indicated that dust was dominant (see yellow areas), corroborating information retrieved from SEVIRI data. It should be remarked that an increase of the electron density and many whistlers (vertical lines), with increased intensities corresponding to the lightning strokes in the atmosphere, characterized the dusty region intersected by the orbit track of DEMETER on 19 May at around 8:08 p.m. UT (see Figure 10).



(a)

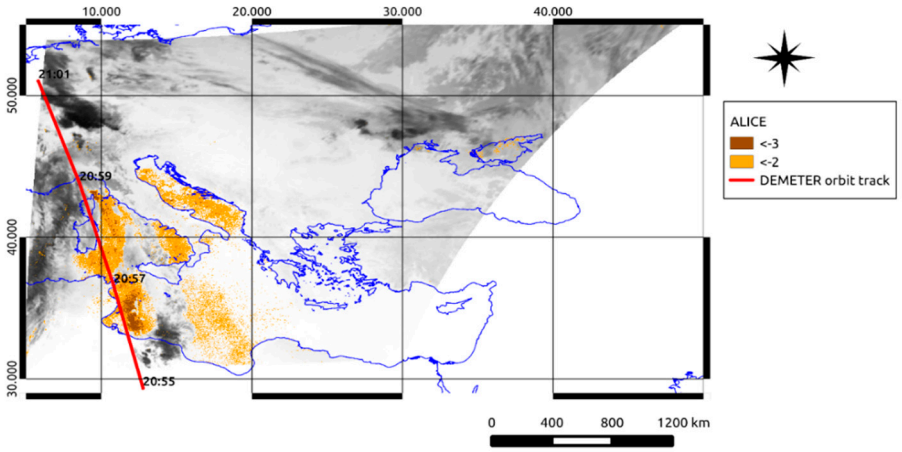


(b)

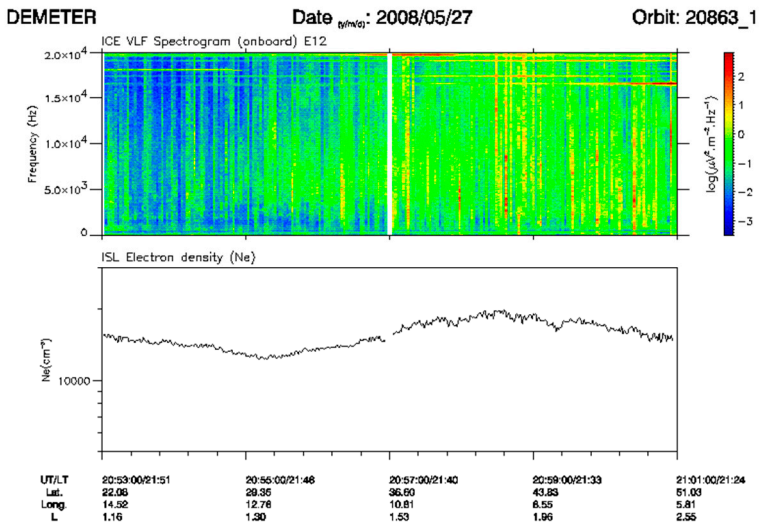
Figure 12. (**a**) Cloud-Aerosol Lidar with Orthogonal Polarization Lidar (CALIOP) lidar profile of 20 May 2008 acquired between 12:29 and 12:43 a.m. UT, along the orbit track of CALIPSO reported in green in Figure 11, showing the presence of an aerosol layer extending up to about 6 km above sea level (a.s.l.) (see black ellipse); (**b**) aerosol subtype profile.

Thus, we can suppose that the dust plume was electrically active and capable of perturbing the ionosphere, such as the following dust event of 26–31 May 2008. Indeed, desert dust affected the same region of the Mediterranean Sea where DEMETER (the orbit track of which is depicted in red in Figure 13a) recorded, on 27 May, an increase in the electron density and thunderstorm activity (see Figure 13b). Also, similar ionospheric disturbances were recorded in the following days when the dust phenomenon was still in progress. In addition, the GIM TEC significantly enhanced over the area affected by Saharan dust both on 19 and 27 May 2008, as indicated by dotted circles in Figure 14, where the top panel is the raw data and the bottom one is the associated STD (Standard Deviation). In detail,

a marked and continuous increase in the electron density was recorded between 8:55 and 8:59 p.m. UT (i.e., just when DEMETER passed over the dusty area identified by RST using SEVIRI data).



(a)

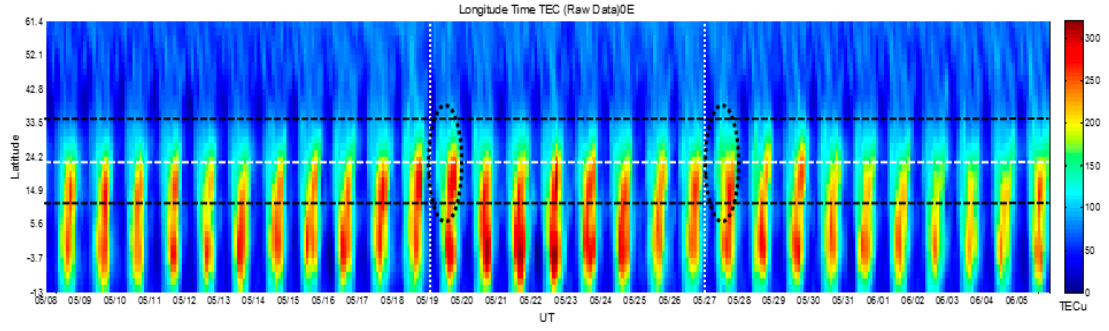


(b)

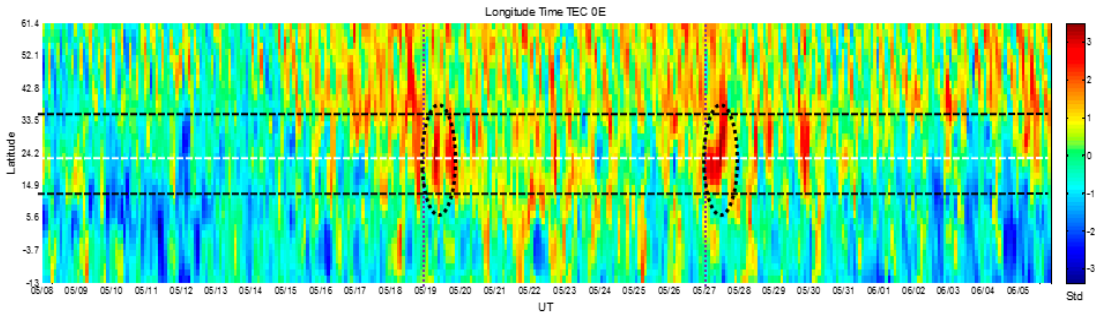
Figure 13. (**a**) RST map of 27 May 2008 at 9:00 p.m. UT, orange and brown pixels as well as the red line have the same meaning as in Figure 11; (**b**) DEMETER data recorded on 27 May 2008 between 8:53:00 and 9:01:00 p.m. UT. On the top, electric VLF spectrogram from 0 up to 20 kHz with its intensity color coded according to the scale on the right. On the bottom, variation of the electron density with the parameters displayed below representing the time in UT and LT, the geographic latitude and longitude, and the McIlwain parameter L.

To investigate the impact of Saharan dust on the ionosphere, we also examined the longitude–time–TEC (LTT) along the 0° E longitude. In addition, we developed TEC for the global fixed local time at 10:00 p.m. for cross-comparison with DEMETER observations. It can be noted that the GIM TEC significantly increased over the Saharan region during the investigated period (i.e., both on 19 and 27 May 2008) (see both panels in Figure 15).

Since the global fixed local time is the TEC at the same local time on a particular day being isolated, the local time effects were removed, allowing us to cross-compare the GIM TEC with the sun-synchronous orbit observations of DEMETER at about 8:00–10:00 p.m. LT, globally.

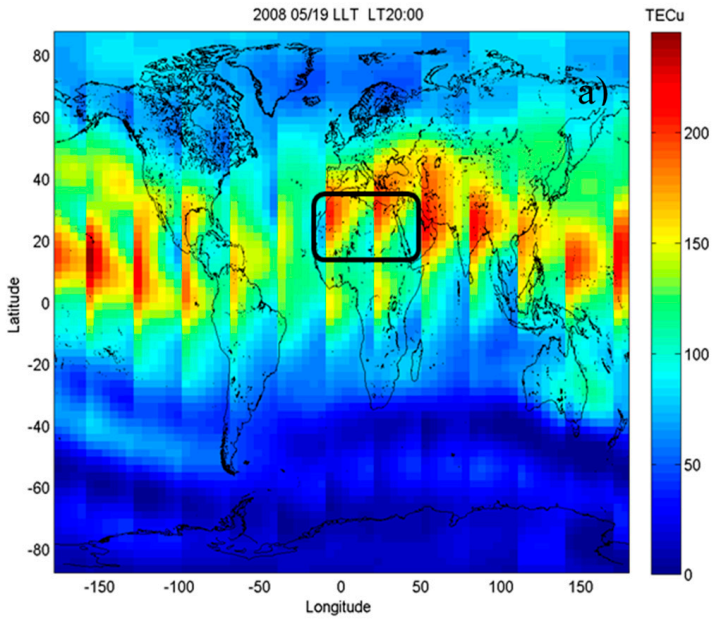


(a)



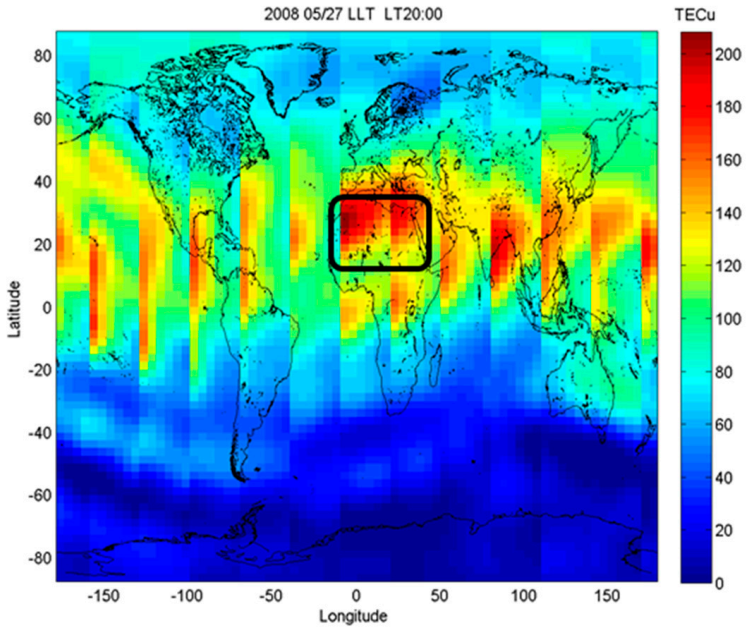
(b)

Figure 14. (**a**) Longitude–time–TEC (LTT) plots extracted from the global ionosphere map (GIM) along the 0° E longitude; (**b**) standardized plot. The mean is computed at each location and each time point for the observation period of 8 May–6 June 2008.



(a)

Figure 15. *Cont.*



(b)

Figure 15. Latitude–longitude (LLT) maps at global fixed local time 8:00 p.m. LT extracted from the GIMs along various longitudes in reference to: (**a**) 19 May 2008; (**b**) 27 May 2008.

7. Discussion

In this work, we investigated the impact of volcanic/Saharan dust events on the ionosphere, analyzing a number of independent observations.

Ionospheric perturbations recorded by DEMETER on 4 November and 6 December 2006 occurred during some intense eruptive events of Mt. Etna. Further, an ash plume, dispersing over the Mediterranean Sea more than 100 km from the eruptive center, affected the same region where, some hours later, DEMETER recorded a significant increase of the ion density. Since volcanic ash may electrically interact with the atmosphere (e.g., [34,96]) and considering that gas emissions, heat flux, and volcanic explosions may also disturb the ionosphere [4,97], the impact of those eruptions on DEMETER observations appears plausible. In support of this hypothesis, the sea region characterized by the ion density increase was spatially close to the Mt. Etna area. Indeed, ionospheric perturbations recorded by DEMETER were within the distance threshold (VEI $\leq$ 3) of 500 km from eruptive centers identified by other authors to assess the possible relation between ionospheric anomalies and eruptive activities [4,5].

Those outcomes fit with results of previous papers, which independently investigated the possible relation between ionospheric perturbations and eruptive activities (e.g., [5,75] and the references herein). In each instance of this study, we can attribute the variation of the ion density to the modification of the GEC, which is present between the Earth's surface and the bottom of the ionosphere [98]. In particular, large amounts of heavy ion clusters, which replace the light ions within the area of a volcano eruption, drastically change the air column conductivity. This leads to the modification of parameters of the GEC, which is responsible for electromagnetic coupling between the ground and ionosphere. It creates the local anomalies of electron concentration and electron and ion temperature within the ionosphere (e.g., [11,99]). DEMETER observations, showing anomalies in the electrical field, coincided with the timing of thermal enhancements on 4 November and 6 December 2006, as revealed by OLR anomalies. The cross-correlation of OLR at TOA and ionospheric anomalies is evidence for the presence of the lithosphere–atmosphere–ionosphere coupling chain triggered by Mt. Etna volcanic activity occurring in 2006. Moreover, due to the plasma characteristics of the quasi-neutrality, which means the number of ions is about equal to that of electrons, the DEMETER ion and the ground-based

GPS TEC simultaneously increased over the Mt. Etna area. Those agreements indicated that the electromagnetic environment around the volcano area was modified during the eruptive periods investigated here.

Regarding the ionospheric disturbances of May 2008, which cannot be associated with Mt. Etna and/or Stromboli eruptions (see previous paragraph), they were possibly determined by two massive dust outbreaks occurring in that period. Those dust events were identified using data from SEVIRI, which offers a synoptic view and a high frequency of observation adequate to monitor spatially distributed and rapidly evolving phenomena. Specifically, RST maps showed that airborne dust affected the same region where DEMETER recorded an increase of the electron density and lightning strokes during May 2008. In this case, it is certainly difficult to attribute a part of the lightning strokes to electrostatic discharges in the dust plume because their intensities could not be so important. Therefore, we can hypothesize that either the dust phenomenon contributed to increasing the number of lightning strokes in the atmosphere or it changed the properties of the bottom of the ionosphere in such a way that the waves were not so attenuated when they crossed the ionosphere to reach the satellite. In addition, the analysis of LTT plots revealed that the ionospheric TEC significantly increased over dusty areas on both 19 and 27 May 2008. Indeed, the global comparison confirms that the GPS TEC mostly increased over the Sahara region, especially on 27 May, showing once again that the GEC was responsible for the electromagnetic coupling between the ground and ionosphere.

8. Conclusions

The results of this study have shown that a multiparametric approach may provide an important contribution for better interpreting the actual origin of ionospheric anomalies. This contribution may be particularly valuable when ionospheric disturbances are investigated as possible indicators of impending earthquakes (e.g., [100–108]). Indeed, the integration of independent observations is nowadays expected to be a major improvement in short-term seismic hazard forecast. The possibility of moving to the operational use of this information, independently obtained by well-established data analysis methodologies (e.g., [61,109–111] and references herein), strongly relies on our present capability in discriminating anomalous transients, possibly related to an impending earthquake, from those related to other natural, and in general nonseismic, sources. This paper, other than confirming the significant impacts on the ionosphere of volcanic eruptions and dust outbreaks, also demonstrates the importance of a multiparametric approach in identifying and removing false-positives in seismic hazard forecast applications. This way, by reducing false alarm rates, the identification of anomalous transients related to volcanic eruptions and/or to dust events could significantly improve the reliability of forecasts based on measurements of single and/or multiple parameters.

Finally, the multiparametric approach used in this study could also have a positive impact on observations from missions such as Swarm, a European Space Agency (ESA) three-satellite constellation enabling the investigation of electric currents flowing in the magnetosphere and ionosphere [112], and the China Seismo-Electromagnetic Satellite (CSES). The latter is a Chinese–Italian space mission for the monitoring of the electromagnetic field and wave, plasma, and particle perturbations of the atmosphere, ionosphere, and magnetosphere induced by natural sources and anthropocentric emitters [113].

Author Contributions: V.T.: writing, coordination, and revision; F.M.: writing and AVHRR/SEVIRI data analyses; A.F.: SEVIRI data analysis and SW development; C.F.: SEVIRI data provision and analysis; N.G.: thermal anomalies and RST products analyses; K.H.: data analyses; M.L.: thermal anomalies and RST products analyses; J.Y.L.: writing and TEC data analyses; D.O.: writing and OLR data analyses; M.P.: writing and DEMETER data analyses; N.P.: writing and RST dust/ash products analyses; S.P.: writing and ACP data analyses.

Funding: The work was partially funded by the SMART BASILICATA project funded by MIUR under the "Smart Cities and Communities and Social Innovation" Call, MIUR Announcement n.84/Ric 2012, PON 2007 – 2013 of 2nd March 2012.

Acknowledgments: DEMETER was a satellite launched by the Centre National d'Etudes Spatiales. This work is based on observations with the electric field instrument ICE, and the density experiments ISL and IAP aboard

DEMETER. The authors thank J. J. Berthelier, the PI of ICE and IAP, and J.P. Lébréton, the PI of ISL for the use of the data. The authors thank ISSI (Bern) for the support of the team "Multi-instrument Space-Borne Observations and Validation of the Physical Model of the Lithosphere-Atmosphere-Ionosphere-Magnetosphere Coupling". The authors thank the NOAA's Climate Prediction Center and NASA's Goddard Global Modeling and Assimilation Office (GMAO) for providing satellite data products. The MSG-SEVIRI data used in this study followed the EUMETSAT data policy and were made available through the license released by the Meteorological Service of the Italian Military Aeronautics. The authors thank the referees for constructive comments devoted to improve the quality of the paper.

Conflicts of Interest: The authors declare no conflict of interest.

References

1. Cheng, K.; Huang, Y.N. Ionospheric disturbances observed during the period of Mount Pinatubo eruptions in June 1991. *J. Geophys. Res.* **1992**, *97*, 16995–17004. [CrossRef]
2. Igarashi, K.; Kainuma, S.; Nishimuta, I.; Okamoto, S.; Kuroiwa, H.; Tanaka, T.; Ogawa, T. Ionospheric and atmospheric disturbances around Japan caused by the eruption of Mount Pinatubo on 15 June 1991. *J. Atmos. Terr. Phys.* **1994**, *56*, 1227–1234. [CrossRef]
3. Zlotnicki, J.; Le Mouël, J.L.; Kanwar, R.; Yvetot, P.; Vargemezis, G.; Menny, P.; Fauquet, F. Ground-based electromagnetic studies combined with remote sensing based on Demeter mission: A way to monitor active faults and volcanoes. *Planet. Space Sci.* **2006**, *54*, 541–557. [CrossRef]
4. Zlotnicki, J.; Li, F.; Parrot, M. Signals recorded by DEMETER satellite over active volcanoes during the period 2004 August–2007 December. *Geophys. J. Int.* **2010**, *183*, 1332–1347. [CrossRef]
5. Zlotnicki, J.; Li, F.; Parrot, M. Ionospheric Disturbances Recorded by DEMETER Satellite over Active Volcanoes: From August 2004 to December 2010. *Int. J. Geophys.* **2013**, *2013*, 530865. [CrossRef]
6. Rozhnoi, A.; Hayakawa, M.; Solovieva, M.; Hobara, Y.; Fedun, V. Ionospheric effects of the Mt. Kirishima volcanic eruption as seen from subionospheric VLF observations. *J. Atmos. Sol.-Terr. Phys.* **2014**, *107*, 54–59. [CrossRef]
7. Piscini, A.; Marchetti, D.; De Santis, A. Multi-parametric climatological analysis associated with global significant volcanic eruptions during 2002–2017. *Pure Appl. Geophys.* **2019**, in press. [CrossRef]
8. Gringel, W.; Rosen, J.M.; Hofmann, D.J. *Electrical Structure from 0 to 30 km Atmospheric Electricity in the Planetary Boundary Layer: The Earth's Electrical Environment*; National Academic Press: Washington, DC, USA, 1986; pp. 166–182.
9. Pulinets, S.A.; Boyarchuk, K.A.; Khegai, V.V.; Kim, V.P.; Lomonosov, A.M. Quasi electrostatic model of atmosphere–thermosphere–ionosphere coupling. *Adv. Space Res.* **2000**, *26*, 1209–1218. [CrossRef]
10. Ulanowski, Z.; Bailey, J.; Lucas, P.W.; Hough, J.H.; Hirst, E. Alignment of atmospheric mineral dust due to electric field. *Atmos. Chem. Phys.* **2007**, *7*, 6161–6173. [CrossRef]
11. Pulinets, S.; Davidenko, D. Ionospheric precursors of earthquakes and global electric circuit. *Adv. Space Res.* **2014**, *53*, 709–723. [CrossRef]
12. Melnik, O.; Parrot, M. Electrostatic discharge in Martian dust storms. *J. Geophys. Res.* **1998**, *103*, 29107–29118. [CrossRef]
13. Stow, C.D. Dust and sand storm electrification. *Weather* **1969**, *24*, 134–140. [CrossRef]
14. Freier, G.D. The electric field of a large dust devil. *J. Geophys. Res.* **1960**, *65*, 3504. [CrossRef]
15. Crozier, W.D. Dust devil properties. *J. Geophys. Res.* **1970**, *75*, 4583–4585. [CrossRef]
16. Kamra, A.K. Measurements of the electrical properties of dust storms. *J. Geophys. Res.* **1972**, *77*, 5856–5869. [CrossRef]
17. Kamra, A.K. Effect of Dust-Raising Winds on the Atmospheric Electric Field. In *Electrical Processes in Atmosphere*; Dolezalek, H., Reiter, R., Eds.; Steinkopff: Darmstadt, Germany, 1977; pp. 168–174.
18. Schmidt, D.S.; Schmidt, R.A.; Dent, J.D. Electrostatic force on saltating sand. *J. Geophys. Res. Atmos.* **1998**, *103*, 8997–9001. [CrossRef]
19. Jackson, T.L.; Farrell, W.M. Electrostatic fields in dust devils: An analog to Mars. *IEEE Trans. Geosci. Remote Sens.* **2006**, *44*, 2942–2949. [CrossRef]
20. Renno, N.O.; Kok, J.F. Electrical activity and dust lifting on Earth, Mars, and beyond. In *Planetary Atmospheric Electricity*; Springer: New York, NY, USA, 2008; pp. 419–434.

21. Zhang, H.F.; Wang, T.; Qu, J.J.; Yan, M.H. An experimental and observational study on the electric effect of sandstorms. *Chin. J. Geophys.* **2004**, *47*, 53–60. [CrossRef]
22. Saunders, C.P.R. Thunderstorm electrification. In *Handbook of Atmospheric Electrodynamics*; Volland, H., Ed.; CRC Press: Boca Raton, FL, USA, 1995; pp. 61–92.
23. Brook, M.C.; Moore, B.; Sigurgeirsson, T. Lightning in volcanic clouds. *J. Geophys. Res.* **1974**, *79*, 472–475. [CrossRef]
24. Brantley, S.R. The eruption of Redoubt volcano, Alaska, December 14, 1989–August 31, 1990, U.S. *Geol. Surv. Circ.* **1990**, *1061*, 33.
25. Paskievitch, J.F.; Murray, T.L.R.; Hoblitt, P.; Neal, C.A. Lightning associated with the August 18, 1992, eruption of Crater Peak vent, Mount Spurr volcano, Alaska. In *The 1992 Eruptions of Crater Peak Vent, Mount Spurt Volcano, Alaska*; Keith, T.E.C., Ed.; US Government Printing Office: Washington, DC, USA, 1995; Volume 2139, pp. 179–182.
26. McNutt, S.R.; Davis, C.M. Lightning associated with the 1992 eruptions of Crater Peak Mount Spurr volcano, Alaska. *J. Volcanol. Geotherm. Res.* **2000**, *102*, 45–65. [CrossRef]
27. Thomas, R.J.; Krehbiel, P.R.; Rison, W.; Edens, H.E.; Aulich, G.D.; Winn, W.P.; McNutt, S.R.; Tytgat, G.; Clark, E. Electrical activity during the 2006 Mount St. Augustine volcanic eruptions. *Science* **2007**, *315*, 1097. [CrossRef] [PubMed]
28. Aizawa, K.; Yokoo, A.; Kanda, W.; Ogawa, Y.; Iguchi, M. Magnetotelluric pulses generated by volcanic lightning at Sakurajima volcano, Japan. *Geophys. Res. Lett.* **2010**, *37*, L17301. [CrossRef]
29. Behnke, S.A.; Thomas, R.J.; McNutt, S.R.; Schneider, D.J.; Krehbiel, P.R.; William, R.; Edens, H.E. Observations of volcanic lightning during the 2009 eruption of Redoubt Volcano. *J. Volcanol. Geotherm. Res.* **2013**, *259*, 214–234. [CrossRef]
30. Behnke, S.A.; Thomas, R.J.; Edens, H.E.; Krehbiel, P.R.; Rison, W. The 2010 eruption of Eyjafjallajökull: Lightning and plume charge structure. *J. Geophys. Res. Atmos.* **2014**, *119*, 833–859. [CrossRef]
31. Antel, C.; Collier, A.B.; Lichtenbergerand, J.; Rodger, C.J. Investigating Dunedin whistlers using volcanic lightning. *Geophys. Res. Lett.* **2014**, *41*, 4420–4426. [CrossRef]
32. James, M.R.; Lane, S.J.; Gilbert, J.S. Volcanic plume electrification: Experimental investigation of a fracture-charging mechanism. *J. Geophys. Res.* **2000**, *105*, 16641–16649. [CrossRef]
33. James, M.R.; Wilson, L.; Lane, S.J.; Gilbert, J.S.; Mather, T.A.; Harrison, R.G.; Martin, R.S. Electrical charging of volcanic plumes. *Space Sci. Rev.* **2008**, *137*, 399–418. [CrossRef]
34. Mather, T.A.; Harrison, R.G. Electrification of volcanic plumes. *Surv. Geophys.* **2006**, *27*, 387–432. [CrossRef]
35. Arason, P.; Bennett, A.J.; Burgin, L.E. Charge mechanism of volcanic lightning revealed during the 2010 eruption of Eyjafjallajökull. *J. Geophys. Res.* **2011**, *116*, B00C03. [CrossRef]
36. McNutt, S.R.; Williams, E.R. Volcanic lightning: Global observations and constraints on source mechanisms. *Bull. Volcanol.* **2010**, *72*, 1153–1167. [CrossRef]
37. Berthelier, J.J.; Godefroy, M.; Leblanc, F.; Seran, E.; Peschard, D.; Gilbert, P.; Artru, J. IAP, the thermal plasma analyzer on DEMETER. *Planet. Space Sci.* **2006**, *54*, 487–501. [CrossRef]
38. Lebreton, J.P.; Stverak, S.; Travnicek, P.; Maksimovic, M.; Klinge, D.; Merikallio, S.; Lagoutte, D.; Poirier, B.; Kozacek, Z.; Salaquarda, M. The ISL Langmuir Probe experiment and its data processing onboard DEMETER: Scientific objectives, description and first results. *Planet. Space Sci.* **2005**, *54*, 472–486. [CrossRef]
39. Berthelier, J.J.; Godefroy, M.; Leblanc, F.; Malingre, M.; Menvielle, M.; Lagoutte, D.; Brochot, J.Y.; Colin, F.; Elie, F.; Legendre, C.; et al. ICE The electric field experiment on DEMETER. *Planet. Space Sci.* **2006**, *54*, 456–471. [CrossRef]
40. Higgins, J.; Harris, A. VAST: A program to locate and analyse volcanic thermal anomalies automatically from remotely sensed data. *Comput. Geosci.* **1997**, *23*, 627–645. [CrossRef]
41. Pergola, N.; Marchese, F.; Tramutoli, V. Automated detection of thermal features of active volcanoes by means of infrared AVHRR records. *Remote Sens. Environ.* **2004**, *93*, 311–327. [CrossRef]
42. Marchese, F.; Filizzola, C.; Genzano, N.; Mazzeo, G.; Pergola, N.; Tramutoli, V. Assessment and improvement of a robust satellite technique (RST) for thermal monitoring of volcanoes. *Remote Sens. Environ.* **2011**, *115*, 1556–1563. [CrossRef]
43. Piscini, A.; Lombardo, V. Volcanic hot spot detection from optical multispectral remote sensing data using artificial neural networks. *Geophys. J. Int.* **2014**, *196*, 1525–1535. [CrossRef]

44. Marchese, F.; Neri, M.; Falconieri, A.; Lacava, T.; Mazzeo, G.; Pergola, N.; Tramutoli, V. The Contribution of Multi-Sensor Infrared Satellite Observations to Monitor Mt. Etna (Italy) Activity during May to August 2016. *Remote Sens.* **2018**, *10*, 1948. [CrossRef]
45. Prata, A.J. Observations of volcanic ash clouds in the 10–12mm window using AVHRR/2 data. *Int. J. Remote Sens.* **1989**, *10*, 751–761. [CrossRef]
46. Prata, A.J. Infrared radiative transfer calculations for volcanic ash clouds. *Geophys. Res. Lett.* **1989**, *16*, 1293–1296. [CrossRef]
47. Francis, P.N.; Cooke, M.C.; Saunders, R.W. Retrieval of physical properties of volcanic ash using Meteosat: A case study from the 2010 Eyjafjallajökull eruption. *J. Geophys. Res.* **2012**, *117*, D00U09. [CrossRef]
48. Prata, A.J.; Prata, A.T. Eyjafjallajökull volcanic ash concentrations determined using Spin Enhanced Visible and Infrared Imager measurements. *J. Geophys. Res. Atmos.* **2012**, *117*, 1–23. [CrossRef]
49. Guéhenneux, Y.; Gouhier, M.; Labazuy, P. Improved space borne detection of volcanic ash for real-time monitoring using 3-Band method. *J. Volcanol. Geotherm. Res.* **2015**, *293*, 25–45. [CrossRef]
50. Li, J.; Zhang, P.; Schmit, T.J.; Schmetz, J.; Menzel, W.P. Technical note: Quantitative monitoring of a Saharan dust event with SEVIRI on Meteosat-8. *Int. J. Remote Sens.* **2007**, *28*, 2181–2186. [CrossRef]
51. Klüser, L.; Schepanski, K. Remote sensing of mineral dust over land with MSG infrared channels: A new Bitemporal Mineral Dust Index. *Remote Sens. Environ.* **2009**, *113*, 1853–1867. [CrossRef]
52. Sannazzaro, F.; Filizzola, C.; Marchese, F.; Corrado, R.; Paciello, R.; Mazzeo, G.; Pergola, N.; Tramutoli, V. Identification of dust outbreaks on infrared MSG-SEVIRI data by using a Robust Satellite Technique (RST). *Acta Astronaut.* **2014**, *93*, 64–70. [CrossRef]
53. Tramutoli, V. Robust AVHRR Techniques (RAT) for Environmental Monitoring: Theory and applications. In *Earth Surface Remote Sensing II, Proceedings of SPIE*; Zilioli, E., Ed.; SPIE Press: Bellingham, WA, USA, 1998; Volume 3496, pp. 101–113.
54. Tramutoli, V. Robust Satellite Techniques (RST) for Natural and Environmental Hazards Monitoring and Mitigation: Theory and Applications. In Proceedings of the 2007 International Workshop on the Analysis of Multi-temporal Remote Sensing Images, Leuven, Belgium, 18–20 July 2007. [CrossRef]
55. Sardón, E.; Rius, A.; Zarrao, N. Estimation of the transmitter and receiver differential biases and the ionospheric total electron content from global positioning system observation. *Radio Sci.* **1994**, *29*, 577–589. [CrossRef]
56. Liu, J.Y.; Tsai, H.F.; Jung, T.K. Total electron content obtained by using the global positioning system. *Terr. Atmos. Ocean. Sci.* **1996**, *7*, 107–117. [CrossRef]
57. Tsai, H.F.; Liu, J.Y. Ionospheric total electron content response to solar eclipses. *J. Geophys. Res.* **1999**, *104*, 12657–12668. [CrossRef]
58. Němec, F.; Santolík, O.; Parrot, M. Decrease of Intensity of ELF/VLF Waves observed in the Upper Ionosphere close to Earthquakes: A Statistical Study. *J. Geophys. Res. Space Phys.* **2009**, *114*, 1–10. [CrossRef]
59. He, Y.; Yang, D.; Qian, J.; Parrot, M. Response of the ionospheric electron density to different types of seismic events. *Nat. Hazards Earth Syst. Sci.* **2011**, *11*, 2173–2180. [CrossRef]
60. Píša, D.; Němec, F.; Santolík, O.; Parrot, M.; Rycroft, M. Additional attenuation of natural VLF electromagnetic waves observed by the DEMETER spacecraft resulting from pre-seismic activity. *J. Geophys. Res. Space Phys.* **2013**, *118*, 5286–5295. [CrossRef]
61. Eleftheriou, A.; Filizzola, C.; Genzano, N.; Lacava, T.; Lisi, M.; Paciello, R.; Pergola, N.; Vallianatos, F. Long-Term RST Analysis of Anomalous TIR Sequences in Relation with Earthquakes Occurred in Greece in the Period 2004–2013. *Pure Appl. Geophys.* **2016**, *173*, 285–303. [CrossRef]
62. Lacava, T.; Filizzola, C.; Pergola, N.; Sannazzaro, F.; Tramutoli, V. Improving flood monitoring by the Robust AVHRR Technique (RAT) approach: The case of the April 2000 Hungary flood. *Int. J. Remote Sens.* **2010**, *31*, 2043–2062. [CrossRef]
63. Grimaldi, C.S.L.; Casciello, D.; Coviello, I.; Lacava, T.; Pergola, N.; Tramutoli, V. An improved RST approach for timely alert and Near Real Time monitoring of oil spill disasters by using AVHRR data. *Nat. Hazards Earth Syst. Sci.* **2011**, *11*, 1281–1291. [CrossRef]
64. Filizzola, C.; Corrado, R.; Marchese, F.; Mazzeo, G.; Paciello, R.; Pergola, N.; Tramutoli, V. Erratum to RST-FIRES, an exportable algorithm for early-fire detection and monitoring: Description, implementation, and field validation in the case of the MSG-SEVIRI sensor. *Remote Sens. Environ.* **2017**, *186*, 196–216. [CrossRef]

65. Marchese, F.; Mazzeo, G.; Coviello, I.; Falconieri, A.; Filizzola, C.; Lacava, T.; Pergola, N.; Tramutoli, V. Issues and possible improvements in winter fires detection by satellite radiances analysis: Lesson learnt in two regions of Northern Italy. *J. Sel. Top. Appl. Earth Obs. Remote Sens.* **2017**, *10*, 3297–3313. [CrossRef]
66. Marchese, F.; Falconieri, A.; Pergola, N.; Tramutoli, V. A retrospective analysis of the Shinmoedake (Japan) eruption of 26–27 January 2011 by means of Japanese geostationary satellite data. *J. Volcanol. Geotherm. Res.* **2014**, *269*, 1–13. [CrossRef]
67. Pergola, N.; Tramutoli, V.; Marchese, F.; Scaffidi, I.; Lacava, T. Improving volcanic ash cloud detection by a robust satellite technique. *Remote Sens. Environ.* **2004**, *90*, 1–22. [CrossRef]
68. Marchese, F.; Sannazzaro, F.; Falconieri, A.; Filizzola, C.; Pergola, N.; Tramutoli, V. An enhanced satellite-based algorithm for detecting and tracking dust outbreaks by means of SEVIRI data. *Rem. Sens.* **2017**, *9*, 537. [CrossRef]
69. Ouzounov, D.; Pulinets, S.; Romanov, A.; Romanov, A.; Tsybulya, K.; Davidenko, D.; Kafatos, M.; Taylor, P. Atmosphere-Ionosphere Response to the M9 Tohoku Earthquake Reviled by Joined Satellite and Ground Observations. *Earthq. Sci.* **2011**, *24*, 557–564. [CrossRef]
70. Ouzounov, D.; Pulinets, S.; Hattori, K.; Taylor, P. *Pre-Earthquake Processes: A Multi-disciplinary Approach to Earthquake Prediction Studies*; AGU/Wiley: Hoboken, NJ, USA, 2018; Volume 385.
71. Ouzounov, D.; Liu, D.; Kang, C.; Cervone, G.; Kafatos, M.; Taylor, P. Outgoing Long Wave Radiation Variability from IR Satellite Data Prior to Major Earthquakes. *Tectonophysics* **2007**, *431*, 211–220. [CrossRef]
72. Tramutoli, V.; Di Bello, G.; Pergola, N.; Piscitelli, S. Robust satellite techniques for remote sensing of seismically active areas. *Ann. Geophys.* **2001**, *44*, 295–312.
73. Tramutoli, V.; Cuomo, V.; Filizzola, C.; Pergola, N.; Pietrapertosa, C. Assessing the potential of thermal infrared satellite surveys for monitoring seismically active areas: The case of Kocaeli (Izmit) earthquake, August 17, 1999. *Remote Sens. Environ.* **2005**, *96*, 409–426. [CrossRef]
74. Hernández-Pajares, M.; Juan, J.; Sanz, J.; Orus, R.; Garcia-Rigo, A.; Feltens, J.; Komjathy, A.; Schaer, S.C.; Krankowski, A. The IGS VTEC maps: A reliable source of ionospheric information since 1998. *J. Geod.* **2009**, *83*, 263–275. [CrossRef]
75. Pulinets, S.; Ouzounov, D.; Karelin, A.V.; Davidenko, D. Physical bases of the generation of short-term earthquake precursors: A complex model of ionization-induced geophysical processes in the lithosphere-atmosphere-ionosphere-magnetosphere system. *Geomagn. Aeron.* **2015**, *55*, 521–538. [CrossRef]
76. Calvari, S.; Neri, M.; Pinkerton, H. Effusion rate estimations during the 1999 summit eruption on Mt. Etna, and growth of two distinct lava flow fields. *J. Volcanol. Geotherm. Res.* **2002**, *119*, 107–123. [CrossRef]
77. Behncke, B.; Neri, M. The July–August 2001 eruption of Mt. Etna (Sicily). *Bull. Volcanol.* **2003**, *65*, 461–476. [CrossRef]
78. Branca, S.; Del Carlo, P. Types of eruptions of Etna volcano AD 1670–2003: Implications for short-term eruptive behavior. *Bull. Volcanol.* **2005**, *67*, 732–742. [CrossRef]
79. Salvi, F.; Scandone, R.; Palma, C. Statistical analysis of the historical activity of Mount Etna, aimed at the evaluation of volcanic hazard. *J. Volcanol. Geotherm. Res.* **2006**, *154*, 159–168. [CrossRef]
80. Del Negro, C.; Cappello, A.; Neri, M.; Bilotta, G.; Hérault, A.; Ganci, G. Lava flow hazards at Mount Etna: Constraints imposed by eruptive history and numerical simulations. *Sci. Rep.* **2013**, *3*. [CrossRef]
81. Neri, M.; Behncke, B.; Burton, M.; Galli, G.; Giammanco, S.; Pecora, E.; Privitera, E.; Reitano, D. Continuous soil radon monitoring during the July 2006 Etna eruption. *Geophys. Res. Lett.* **2006**, *33*, L24316. [CrossRef]
82. Andronico, D.; Scollo, S.; Cristaldi, A.; Ferrari, F. Monitoring ash emission episodes at Mt. Etna: The 16 November 2006 case study. *J. Volcanol. Geotherm. Res.* **2009**, *180*, 123–134. [CrossRef]
83. Global Volcanism Program. Report on Etna (Italy). In *Bulletin of the Global Volcanism Network 31:10, Smithsonian Institution*; Wunderman, R., Ed.; Global Volcanism Program: Washington, DC, USA, 2006; Available online: http://volcano.si.edu/showreport.cfm?doi=10.5479/si.GVP.BGVN200610-211060 (accessed on 17 January 2019).
84. Global Volcanism Program. Report on Etna (Italy). In *Bulletin of the Global Volcanism Network 31:8, Smithsonian Institution*; Wunderman, R., Ed.; Global Volcanism Program: Washington, DC, USA, 2006; Available online: https://doi.org/10.5479/si.GVP.BGVN200608-211060 (accessed on 12 April 2019).
85. Andronico, D.; Spinetti, C.; Cristaldi, A.; Buongiorno, M.F. Observations of Mt. Etna volcanic ash plumes in 2006: An integrated approach from ground-based and polar satellite NOAA–AVHRR monitoring system. *J. Volcanol. Geotherm. Res.* **2009**, *180*, 135–147. [CrossRef]

86. Amiridis, V.; Kafatos, M.; Perez, C.; Kazadzis, S.; Gerasopoulos, E.; Mamouri, R.E.; Papayannis, A.; Kokkalis, P.; Giannakaki, E.; Basart, S.; et al. The Potential of the Synergistic Use of Passive and Active Remote Sensing Measurements for the Validation of a Regional Dust Model. *Ann. Geophys.* **2009**, *27*, 3155–3164. [CrossRef]
87. Bègue, N.; Tulet, P.; Chaboureau, J.P.; Roberts, G.; Gomes, L.; Mallet, M. Long-range transport of Saharan dust over northwestern Europe during EUCAARI 2008 campaign: Evolution of dust optical properties by scavenging. *J. Geophys. Res.* **2012**, *117*, D17201. [CrossRef]
88. Wiegner, M.; Groß, S.; Freudenthaler, V.; Schnell, F.; Gasteiger, J. The May/June 2008 Saharan dust event over Munich: Intensive aerosol parameters from lidar measurements. *J. Geophys. Res. Atmos.* **2011**, *116*. [CrossRef]
89. Klein, H.; Nickovic, S.; Haunold, W.; Bundke, U.; Nillius, B.; Ebert, M.; Weinbruch, S.; Schuetz, L.; Levin, Z.; Barrie, L.A.; et al. Saharan dust and ice nuclei over Central Europe. *Atmos. Chem. Phys.* **2010**, *10*, 14993–15022. [CrossRef]
90. Piscini, A.; Corradini, S.; Marchese, F.; Merucci, L.; Pergola, N.; Tramutoli, V. Volcanic ash cloud detection from space: A comparison between the RSTASH technique and the water vapour corrected BTD procedure. *Geomat. Nat. Hazards Risk* **2011**, *2*, 263–277. [CrossRef]
91. Falconieri, A.; Cooke, M.C.; Filizzola, C.; Marchese, F.; Pergola, N.; Tramutoli, V. Comparing Two Independent Satellite-Based Algorithms for Detecting and Tracking Ash Clouds by Using SEVIRI Sensor. *Sensors* **2018**, *18*, 369. [CrossRef]
92. Global Volcanism Program. Report on Etna (Italy). In *Bulletin of the Global Volcanism Network 33:5, Smithsonian Institution*; Wunderman, R., Ed.; Global Volcanism Program: Washington, DC, USA, 2008; Available online: http://dx.doi.org/10.5479/si.GVP.BGVN200805-211060 (accessed on 17 January 2019).
93. Istituto Nazionale di Geofisica e Vulcanologia (INGV). *Rapporto Settimanale Sull'Attività Eruttiva dello Stromboli Ripresa Dalle Telecamere di Sorveglianza*, 19–25 Maggio 2008. Available online: http://www.ct.ingv.it/it/avvisi-e-bandi/doc_view/288-rapporto-settimanale-sull-attivita-eruttiva-dello-stromboli-ripresa-dalle-telecamere-di-sorveglianza.html (accessed on 17 January 2019). (In Italian).
94. Global Volcanism Program. Report on Etna (Italy). In *Weekly Volcanic Activity Report*; Sennert, S.K., Ed.; US Geological Survey: Reston, VA, USA, 2008.
95. National Aeronautics and Space Administration. The Cloud-Aerosol Lidar and Infrared Pathfinder Satellite Observation (CALIPSO). Available online: https://www-calipso.larc.nasa.gov/ (accessed on 1 March 2019).
96. Liperovsky, V.A.; Meister, C.V.; Liperovskaya, E.V.; Davidov, V.F.; Bogdanov, V.V. On the possible influence of radon and aerosol injection on the atmosphere and ionosphere before earthquakes. *Nat. Hazards Earth Syst. Sci.* **2005**, *5*, 783–789. [CrossRef]
97. Heki, K. Explosion energy of the 2004 eruption of the Asama Volcano, central Japan, inferred from ionospheric disturbances. *Geophys. Res. Lett.* **2006**, *33*, L14303. [CrossRef]
98. Rycroft, M.J.; Harrison, R.G. Electromagnetic atmosphere-plasma coupling: The global atmospheric electric circuit. *Space Sci. Rev.* **2012**, *168*, 363–384. [CrossRef]
99. Pulinets, S.; Ouzounov, D. Lithosphere–Atmosphere–Ionosphere Coupling (LAIC) model–An unified concept for earthquake precursors validation. *J. Asian Earth Sci.* **2011**, *41*, 371–382. [CrossRef]
100. Parrot, M.; Achache, J.; Berthelier, J.J.; Blanc, E.; Deschamps, A.; Lefeuvre, F.; Menvielle, M.; Plantet, J.L.; Tarits, P.; Villain, J.P. High-frequency seismo-electromagnetic effects. *Phys. Earth Planet. Inter.* **1993**, *77*, 65–83. [CrossRef]
101. Parrot, M.; Berthelier, J.J.; Lebreton, J.P.; Sauvaud, J.A.; Santolik, O.; Blecki, J. Examples of unusual ionospheric observations made by the DEMETER satellite over seismic regions. *Phys. Chem. Earth* **2006**, *31*, 486–495. [CrossRef]
102. Hayakawa, M. Electromagnetic Precursors of Earthquakes: Review of Recent Activities. *Rev. Radio Sci. 1993–1995* **1997**, 807–818.
103. Molchanov, O.A.; Rozhnoi, A.; Solovieva, M.; Akentieva, O.; Berthelier, J.J.; Parrot, M.; Lefeuvre, F.; Biagi, P.F.; Castellana, L.; Hayakawa, M. Global diagnostics of the ionospheric perturbations related to the seismic activity using the VLF radio signals collected on the DEMETER satellite. *Nat. Hazards Earth Syst. Sci.* **2006**, *6*, 745–753. [CrossRef]
104. Sarkar, S.; Gwal, A.K.; Parrot, M. Ionospheric variations observed by the DEMETER satellite in the mid-latitude region during strong earthquakes. *J. Atmos. Sol.-Terr. Phy.* **2007**, *69*, 1524–1540. [CrossRef]

105. Muto, F.; Yoshida, M.; Horie, T.; Hayakawa, M.; Parrot, M.; Molchanov, A. Detection of ionospheric perturbations associated with Japanese earthquakes on the basis of reception of LF transmitter signals on the satellite DEMETER. *Nat. Hazards Earth Syst. Sci.* **2008**, *8*, 135–141. [CrossRef]
106. Slominska, E.; Blecki, J.; Parrot, M.; Slominski, J. Satellite study of VLF ground-based transmitter signals during seismic activity in Honshu Island. *Phys. Chem. Earth* **2009**, *34*, 464–473. [CrossRef]
107. De Santis, A.; De Franceschi, G.; Spogli, L.; Perrone, L.; Alfonsi, L.; Qamili, E.; Cianchini, G.; Di Giovambattista, R.; Salvi, S.; Filippi, E.; et al. Geospace perturbations induced by the earth the state of the art and future trends. *Phys. Chem. Earth* **2015**, *85*, 17–33. [CrossRef]
108. De Santis, A.; Balasis, G.; Pavón-Carrasco, F.J.; Cianchini, G.; Mandea, M. Potential earthquake precursory pattern from space: The 2015 Nepal event seen by magnetic Swarm satellites. *EPSL* **2017**, *461*, 119–126. [CrossRef]
109. Liu, J.Y.; Chen, Y.I.; Chuo, Y.J.; Chen, C.S. A statistical investigation of pre-earthquake ionospheric anomaly. *J. Geophys. Res.* **2006**, *111*. [CrossRef]
110. Li, M.; Parrot, M. Statistical analysis of an ionospheric parameter as a base for earthquake prediction. *J. Geophys. Res. Space Phys.* **2013**, *118*, 3731–3739. [CrossRef]
111. Han, P.; Hattori, K.; Hirokawa, M.; Zhuang, J.; Chen, C.-H.; Febriani, F.; Yamaguchi, H.; Yoshino, C.; Liu, J.-Y.; Yoshida, S. Statistical analysis of ULF seismomagnetic phenomena at Kakioka, Japan, during 2001–2010. *J. Geophys. Res. Space Phys.* **2014**, *119*, 4998–5011. [CrossRef]
112. European Space Agency. Available online: https://earth.esa.int/web/guest/missions/esa-operational-eo-missions/swarm (accessed on 12 April 2019).
113. CSES - China Seismo Electromagnetic Satellite. Available online: http://cses.roma2.infn.it/ (accessed on 12 April 2019).



© 2019 by the authors. Licensee MDPI, Basel, Switzerland. This article is an open access article distributed under the terms and conditions of the Creative Commons Attribution (CC BY) license (http://creativecommons.org/licenses/by/4.0/).